2020-02-15

Quantifying the transient landscape response to active faulting using fluvial geomorphic analysis in the Qianhe Graben on the southwest margin of Ordos, China

Liu, Z

10.1016/j.geomorph.2019.106974
Geomorphology
Elsevier

Quantifying the transient landscape response to active faulting using fluvial geomorphic analysis in the Qianhe Graben on the southwest margin of Ordos, China

Zhiheng Liu[a,b], Ling Han[a,*], Sarah J. Boulton[b], Tingting Wu[a], Jianhua Guo[c]

[a] School of Geology Engineering and Geomatics, Chang'an University, Xi'an 710064, China

[b] School of Geography, Earth and Environmental Sciences, University of Plymouth, Plymouth PL4 8AA, UK

[c] School of Electrical and Information Engineering, Tianjin University, Tianjin 300072, China

* Correspondence to: hanling@chd.edu.cn (Ling Han)

ABSTRACT:

River morphology has been widely used to record and track the transient landscape response to active faulting. Here we evaluate the landscape response to active faulting in the Qianhe Graben of southwest Ordos, China. In this region, it has been difficult to determine the activity of mapped faults because of the presence of thick Quaternary Loess; however, by analysing the presence and distribution of slope-break knickpoints in river longitudinal profiles, the ongoing tectonic uplift of the Qianhe Graben can be investigated. The alignment of vertical-step knickpoints gives a new insight into the location of an active fault on the southern margin of Qianhe Graben. Additionally, slope-break knickpoints, typical of fault controlled landscape change, were identified from 24 river longitudinal profiles that drain across normal faults along both graben margins. Along strike from north to south, the knickpoints varied systematically with relief, and the height of the knickpoints also decrease to the southeast. Indicating that the rate of motion on the faults, likely is greater in the northwest and decays southeastwards. The horizontal knickpoint retreat rates range from 0.3 - 27.3 mm/yr, constraining the landscape response time with fault initiation at 1.2 ~ 1.4 Myr. In comparison with other studies, the knickpoint recession triggered by base-level fall as a result of faulting is relatively lower than when the base-level fall is the result of sea-level fall potentially the result of different mechanism of retreat. Finally, the potential for earthquakes along the Taoyuan-Guichuansi Fault (TGF) before and after fault linkage was assessed, indicating the potential for earthquakes of M_w of 6.3 - 6.7 and

6.8 - 7.0, respectively. These observations not only suggest the knickpoints are recording fault evolution in Qianhe Graben, but also provide information on seismic hazard in this populous region.

KEYWORDS: Qianhe Graben; knickpoint; active faulting; transient landform response

1 Introduction

Tectonic geomorphology is the investigation of the interaction between active tectonics and surface processes, reflecting the coupling relationship between deep geophysical structures and climate processes. Tectonic geomorphic landforms record the landscape response to the spatial distribution of active faults (Kirby et al., 2003; Boulton and Whittaker, 2009; Kirby and Ouimet, 2011; Ozkaymak and Sözbilir, 2012; Hergarten et al., 2016; Topal et al., 2016; Dong et al., 2017; Owen et al., 2017). In bedrock fluvial systems, rivers are sensitive to changes in boundary conditions, such as structure, climate and lithology (Kirby et al., 2003; Whittaker, 2012; Whittaker and Boulton, 2012; Allen et al., 2013; Cyr et al., 2014), and transmit the signal of tectonic and climatic change to the surrounding landscape by setting the landscape response time (Whipple and Tucker, 1999; Kirby et al., 2003). Furthermore, rivers are an effective way to track neo-tectonic movement and topographic evolution (Whipple and Tucker, 1999; Jiang et al., 2016). Previous studies have demonstrated that fluvial geomorphologic parameters can record uplift rates, give insights into active faults, and quantitatively study the external morphological characteristics formed by the internal dynamic geological process (e.g., Whipple and Meade, 2006; Whipple, 2009; Castelltort et al., 2012; Kirby and Whipple, 2012; Boulton et al., 2014; Schanz and Montgomery, 2016; Kent et al., 2017). As a result, fluvial morphologic indices of river longitudinal profiles have become a widespread and easily implemented method to study faulting in active tectonic regions, characterised by transient landscapes responding to boundary condition perturbation (Whipple, 2002; Whittaker et al., 2008;

71 Ozkaymak and Sözbilir, 2012; Whittaker and Boulton, 2012; Faghih et al., 2015; Yan
72 et al., 2015; Matoš et al., 2016; Topal et al., 2016; Tepe and Sözbilir, 2017).
73
74 In some locations, owing to the existence of various limitations, such as thick
75 Quaternary sequences or physical (in)accessibility, it can be difficult to directly
76 measure the slip rate of faults. For example, the Qianhe Graben is a Cenozoic faulted
77 basin covered by thick extensional/transtensional deposits of Quaternary loess (~ 100
78 - 120 m thick) (Fan et al, 2016), located at the intersection of the Liupanshan Fault
79 (LPSF) and Qinling Fault (KLF) in China (Fan et al., 2018; Zhang et al., 2019) (Fig.
80 1b). The thick loess and high relief make the area difficult to explore in the field, and
81 most recent research has focused on applying traditional methods (e.g., hypsometric
82 integral, stream length-gradient index, valley floor width-to-height ratio) (Chen et al.,
83 2003; Cheng et al., 2018; Zhang et al., 2019) to reveal the geomorphic effect of the
84 faults. However, such methods cannot constrain rates of faulting or the rate of
85 landscape response to changing base level. To address this challenge, stream profile
86 analysis offers an alternative method to investigate neotectonic deformation, and the
87 growth and linkage of faults of the study area (Kirby et al., 2003; Wobus et al., 2006;
88 Boulton and Whittaker, 2009; Kirby and Whipple, 2012; Boulton et al., 2014; Kent et
89 al., 2017). In transient landscapes, knickpoint (the point in the long profile where the
90 rate of change of channel gradient reaches local maximum) (Haviv et al., 2010;
91 Whittaker and Boulton, 2012; Kent et al., 2016) characteristics and normalized channel
92 steepness (k_{sn}) can be used to investigate fault slip rate and rock uplift rate by

93 analysing digital elevation models (DEMs) (Snyder et al., 2000; Bishop et al., 2005;
94 Crosby and Whipple, 2006; Castillo et al., 2014; Castillo, 2017; Gailleton et al., 2019;
95 Robustelli, 2019). Therefore, in the absence of direct geodetic constraints in active
96 settings much information can be gained through the investigation of knickpoint
97 characteristics, giving new insights into active faulting.
98
99 In this study, the fluvial morphologic indices of longitudinal profiles in Qianhe Graben
100 are extracted to investigate the landscape response to active faults based on digital
101 elevation model (DEM) and GIS spatial analyses. Specifically, the main purposes of
102 this study are: (1) to investigate the topographic response to active faulting by
103 identifying the styles of knickpoints from river longitudinal profiles; (2) to quantify the
104 transient fluvial landscape response to active faulting in this area; (3) to evaluate
105 present and future earthquake hazard in the study area.
106
107 **2 Geological background**
108 The Qianhe Graben is the westernmost extent of the Weihe Graben, located at the
109 intersection between the southwest margin of the Ordos block, the southeastern
110 Liupan-Longxi Plateau, and the northern Qinling fold system (Fig. 1). The palaeo-
111 surface of the study area is buried by Quaternary loess, 100 - 120 m thick (Fan et al.,
112 2016), but bedrock sedimentary strata are exposed dating from the Precambrian to
113 Neogene. The graben is defined by a number of active faults (Wang et al., 2011; Li et
114 al., 2013; Guo et al., 2016; Dong et al., 2017; Chen et al., 2018b; Cheng et al., 2018;

115 Zhang et al., 2019), with four main NW-SE trending active faults; the Taoyuan-
116 Guchuansi Fault (TGF), the Guguan-Guozhen Fault, (GGF), the Qianyang-Biaojiao
117 Fault (QBF), and the Qishan-Mazhao Fault (QMF), and the minor fault Qinling Fault
118 (QLF) (Fig. 1c).
119
120 Previous studies have shown that earthquakes occur frequently in the study area (Fan
121 et al., 2018), and the possibility of large earthquakes (> M_w 6.0) is high (Cheng et al.,
122 2014). However, according to the existing seismicity data (Fig. 1c), the earthquakes
123 that have affected the region during the instrumental period (from 1990 to present) are
124 smaller, < M_w 5.5, while most are ≤ M_w 2.0. Even the 1556 Huaxian earthquake (M_w
125 8.5) and 1704 Longxian earthquake (M_w 6.0) (Fig. 1a, b), which occurred relatively
126 close to the study area, were over 300 years ago (Cheng et al., 2014; Hou et al., 1998).
127 Little information exists on the rates of fault slip. However, since 1.2 ~ 1.4 Ma, the
128 Quaternary activity with average slip rate on the QMF has been estimated, through a
129 combination of palaeoseismology, geomorphology, and deformation survey, as ~ 0.03
130 - 1.50 mm/yr, while GGF slip rate is ~ 0.03 mm/yr (Shi, 2011; Lin et al., 2015). Along
131 the southern margin of the Ordos block, fault activity has increased since 5 Ma owing
132 to the rapid uplift (2.94 ± 0.15 mm/yr) of the Qinling Mountains (Li et al., 2012) and
133 rifting of the Weihe Basin (Ren et al., 2015).
134
135 The active faults bound regions of distinct bedrock lithology. More than 50% of the
136 study area is Quaternary loess (Fig. 1c). To the north of the QMF, the bedrock is

137 composed of red sandstone and conglomerate forming the southwest margin of Ordos
138 block. These sedimentary rocks were deposited during the Jurassic to Cretaceous (Li
139 et al., 2013) and are exposed in river valleys that have incised through the overlying
140 loess. To the east of the GGF are Neogene, Ordovician and Cambrian marbles and
141 limestones, which were exposed by the extrusion of the Longxi block (Fan et al., 2003;
142 Lin et al., 2011; Liang et al., 2014), and to the west of GGF, there are outcrops of
143 Cretaceous conglomerates and sandstone. By contrast, to the west of TGF is a large
144 area of late Paleozoic and post-Triassic red granite (Fig. 1c).
145

146 In addition, there are distinct geomorphic regions within the study area controlled by
147 fault location and behaviour. Across the study area, the topography gradually
148 decreases in elevation from northwest to southeast (Fig. 2a). The highest points in the
149 northwest are composed of lower Paleozoic metamorphic rocks and Paleozoic
150 intermediate-acid intrusive rocks at altitudes of 1800 - 2200 m. The neotectonic uplift
151 driving topographic evolution has resulted in deep valleys and the steep ridges, which
152 form the watershed of the Weihe tributaries. By contrast, the low relief landscape of
153 the southeast gradually merges into the Weihe basin at an altitude of 600 - 700 m (Fig.
154 2a).

155 Since the late Cenozoic, in the Qianhe fault zone between the QMF and the QBF, five
156 asymmetric river terrace levels have developed along the Qianhe River (Sun, 2005;
157 Chen et al., 2018b) (Fig. 2a). Each terrace is composed of alluvial deposits and

158 covered by loess deposits, but the isochrones of paleosol sequences can be
159 accurately recognized (Zhang et al., 2019). The age of the terraces was determined
160 by magnetostratigraphic dating and field work (Chen et al., 2018b; Zhang et al. 2019),
161 providing ages for each terrace (T1 to T5): 0.01, 0.01 - 0.13, 0.12 - 0.60, 0.62 - 0.82,
162 and 1.2 - 1.4 Myrs, respectively (Li, 1991; Fan et al., 2018; Zhang et al., 2019).
163 Therefore, the oldest terrace provides a minimum age for the development of the
164 graben.
165
166 As shown in Figs. 2b, c, and d, three 100 km long strip profiles (AA', BB', CC')
167 perpendicular to the Qianhe fault zone were selected from northwest to southeast for
168 topographic and geomorphologic analysis of the Qianhe basin. It is clear that the TGF
169 and QMF faults are controlling the topography and form the major basin bounding
170 faults of Qianhe basin, which exhibits a basin and range-type topography. Under the
171 interaction of the four faults, the uplifted horsts and adjacent grabens, form the tectonic
172 structure of the region (Fig. 2e). Therefore, it is expected that the morphology of the
173 rivers crossing the Qianhe Graben will record evidence of river evolution and tectonic
174 uplift, providing a dataset for the study of the active faults.
175
176 **3 Method and data collection**
177 That stream profiles can provide insights to tectonic uplift has been confirmed for many
178 years (Hack, 1973; Howard and Kerby, 1983). Rivers in areas of active faulting not
179 only modify their topography to the regional base-level but also set boundary

conditions for the erosion and evolution of adjacent hillslopes (Castillo et al., 2017). Therefore, a simple and efficient method of using river geomorphology to describe bedrock channel forms and processes can reveal much information on the underlying physical processes.

3.1 River erosion model

In order to analyze the fluvial geomorphic response of rivers to tectonic uplift in the study area, a power law function of drainage area *A* and river channel slope *S* is used as follows (Howard and Kerby, 1983; Whipple and Tucker, 1999; Kirby and Whipple, 2001; Bishop et al., 2005; Berlin and Anderson, 2007; Castillo et al., 2017; Scherler et al., 2017):

$$E = K \times A^m \times S^n \quad (1)$$

Where *E* us the detachment-limited rate of bedrock channel erosion; *K* is erosion coefficient related to lithologies, active faults, base level and climate; *m* and *n* are constants.

In steady-state landscape, where the erosion equals uplift, the channel gradient can be solved by Equation 1 for slope giving Equation 2:

$$S = (\frac{U}{K})^{\frac{1}{n}} A^{-\frac{m}{n}} \quad (2)$$

Where m/n represents the concavity, U is uplift rate, and the coefficient $(U/K)^{1/n}$ represents the steepness.

To facilitate this calculation, the river hydraulic erosion model deduced from Equation 2 has been formed and widely used, along with the analysis of stream gradient and drainage area, in the study of tectonic geomorphology (Hack, 1973; Howard et al., 1994; Whipple, 2004; Boulton and Whittaker, 2009; Allen et al., 2013; Regalla et al., 2013; Kale et al., 2014; Nexer et al., 2015; Kent et al., 2017; Sembroni and Molin, 2018), thus:

$$S = k_s A^{-\theta} \tag{3}$$

$$k_s = (\frac{U}{K})^{\frac{1}{n}} \tag{4}$$

$$\theta = \frac{m}{n} \tag{5}$$

Where θ is the concavity index, and k_s is the steepness index.

The θ describes the rate of change of local channel slope and is generally between 0.3 and 0.6 in steady-state rivers (Hack, 1973). Changes in k_s can be used to investigate the uplift rate if there is no significant lithologic variation and sediment erosion (Snyder et al., 2000; Kirby and Whipple, 2012; Xue et al., 2018). Both k_s and θ can be obtained by a linear regression from log-log slope-drainage area plots for study rivers.

In such analyses, it has become an accepted approach to calculate a normalized steepness index (k_{sn}) by using a reference θ, to avoid the strong correlation of k_s and

θ (Kirby and Whipple, 2012; Azañón et al., 2015). Generally, 0.45 is chosen as the reference concavity index θ_{ref}. Therefore, the Equation 3 can be reformed as follows:

$$S = k_{sn} A^{-\theta_{ref}} \quad (6)$$

Not all rivers are in 'steady-state', and river longitudinal profiles can exhibit slope discontinuities (knickpoints). A knickpoint is evidence of the transient state of the river, and divides the channel into two parts with different steepness. Depending on the shape of the knickpoints on a SA plot (Fig. 3), they can be divided into vertical-step type knickpoints and slope-break type knickpoints (Wobus et al., 2006; Haviv et al., 2010; Kirby and Whipple, 2012). A slope-break knickpoint separates downstream incision from the upstream channel yet to respond to changes in boundary conditions. It has been found that when such knickpoints are produced by a singular base-level fall, knickpoints move at the same retrogression rate proportional to the upstream area, causing the knickpoints of different rivers to be at the same altitude (Crosby and Whipple, 2006; Berlin and Anderson, 2007). By contrast, the elevation of knickpoints can scale with fault slip rate on a bounding faults, where multiple river cross a single structure (Boulton and Whittaker, 2009; Whittaker and Boulton, 2012).

Generally, a vertical-step knickpoint is related to a change bedrock strength, which appears at a lithologic boundary, fault zone or densely jointed zone, and the possibility of migration to upstream is limited (Whipple et al., 2013; Wang et al., 2015). Although the knickpoints formed by lithologic differences are generally considered fixed, the

238 channel is also divided into upper and lower parts, but there is little to no variation in
239 k_{sn} across the knickpoints.
240
241 Therefore, vertical-step knickpoints may have limited tectonic significance, while
242 slope-break knickpoints can represent local uplift caused by enhanced tectonic
243 movement (Fig. 3c and d), such as the initiation of faulting or an increase in slip on a
244 fault. Therefore, knickpoint analysis is a useful way to locate structures and analyse
245 geomorphologic evolution (Harkins et al., 2007; Boulton and Whittaker, 2009; Wang et
246 al., 2015; Chen et al., 2018a).
247
248 **3.2 River longitudinal profile**
249 In the absence of knickpoints, it has been proposed that further information on
250 boundary processes can be gained from the shape of the longitudinal profile (Chen et
251 al., 2006; Dong et al., 2017). Steady-state conditions require that uplift = erosion and
252 as a result the elevation of the bedrock channel is invariant. However, if the uplift rate
253 is not equal to the river erosion rate, the steady-state will be broken by the increase in
254 one of the two rates. If the uplift rate is higher, and the river elevation increases along
255 longitudinal profile with respect to time (dz/dt >0) then the linear relationship will
256 transform into concave downward curve (Fig. 4a). By contrast, there will be an upward
257 concave curve when uplift rate < erosion (Chen et al., 2006). Based on Equation 3
258 above, we obtain logarithms on both sides as follows:

$$\log(S) = -\theta \times \log(A) + \log(k_s) \quad (7)$$

For steady-state profiles, the log(S) curve is in a straight line. Then, the log(S) curve is convex when the uplift rate is greater. By contrast, the curve tends to be concave (Fig. 4a), where uplift rates are lower.

According to the results of previous studies (e.g., Ohmori, 1991; Chen et al., 2003; Rãdoane et al., 2003), the shape of the river profiles can also be categorized. The elevation Y of river longitudinal profile changes with the length X, and the profile can be categorised as linear, exponential, logarithmic or power function type related to different stages of landscape evolution (Chen et al., 2006; Dong et al., 2017) (Fig. 4b):

(1) Following surface uplift in tectonically active areas, the concavity of river longitudinal profile can expressed as linear distribution ($Y=a-bX$);

(2) Where river incision is high, material is eroded from the upper and middle reaches and transported to the lower reaches where sediment accumulates. As a result, the curvature of the upper and middle reaches becomes larger, gradually developing an exponential form ($Y=ae^{bX}$);

(3) Continuing erosion and deposition can further accentuate the profile curvature resulting in a transition to the logarithmic profile-type ($Y=a\log X+b$);

(4) Under the influence of regional climate, bedrock fracture and other factors, loose sediment is difficult to retain, the river erosion reaches a maximum, and the concavity of longitudinal profile evolves into a power function ($Y=aX^{b}$).

In summary, the use of the geometric changes in the steady-state river longitudinal profile can provide additional insights into the geomorphological evolution of a region and provide a deeper understanding of the regional tectonic uplift in the absence of knickpoints.

3.3 Data collection

The digital elevation model (DEM) data used here is the Shuttle Radar Topography Mission (SRTM) DEM, which spans the 60°N to 56°S regions of the Earth's surface from a radar topographic survey carried out jointly by National Aeronautics and Space Administration (NASA) and National Imagery and Mapping Agency (NIMA), USA (Hancock et al., 2006). This dataset covers 80% of the land surface, and the DEM is provided as SRTM1 (1"× 1") and SRTM3 (3"× 3") data types, corresponding to the grid resolution of 30 and 90 *m*, respectively. Fortunately, free access to the 1 arc sec data is now available for the research area through the USGS Earth Explorer interface (https://earthexplorer.usgs.gov). Previous research results have shown that SRTM can be used in river hydrological analysis and is superior to ASTER-GDEM (Farr et al., 2007; Arrowsmith and Zielke, 2009; Kirby and Whipple, 2012; Boulton and Stokes, 2018; Wang et al., 2018b). ArcGIS 10.2 software was used to reproject the DEM into WGS_1984_UTM_Zone_48N, convert DEM data, splicing, filling holes, etc., to produce the final DEM of Qianhe Graben (Fig. 2a).

302 The horizontal and vertical accuracy of the STRM DEM is > 99 % (Dong et al., 2017;
303 Farr et al., 2007), which has not limited the interpretation of tectonic landforms in the
304 region. Using the ArcHydrology toolbox and a MATLAB script program (StreamProfiler;
305 Whipple et al., 2007) to extract the river longitudinal profile and watershed catchment
306 area from SRTM data, the river slope can be calculated (Kirby and Whipple, 2012;
307 Zahra et al., 2017). The river channel morphology can be assessed by SA regression
308 to obtain concavity and steepness. The presence or absence of knickpoints can be
309 determined, shaping the subsequent analysis of knickpoint distribution or the shape of
310 the longitudinal profile (Figs. 3 and 4).
311

312 ## 4 Results

313 Using ArcGIS 10.2, twenty-four river long-profiles from the Qianghe Graben were
314 extracted from the SRTM DEM. All tributaries are symmetrically distributed on both
315 sides of the main channel of the Qianhe and Jinlinghe Rivers. Twenty-three of them
316 cross TGF and QMF (Fig. 5). The longitudinal profile form and SA plots reveal
317 information regarding the underlying controls on river formation and elevation (Berlin
318 and Anderson, 2007; Harkins et al., 2007; Whittaker et al., 2007; Stokes et al., 2008;
319 Kirby and Whipple, 2012; Boulton et al., 2014; Giletycz et al., 2015), and record the
320 geomorphic constraints on uplift history (Olivetti et al., 2012; Rossi et al., 2017;
321 Robustelli, 2019). Therefore, the presence or absence of knickpoints was firstly
322 identified, allowing the subsequent analysis to be undertaken appropriately on the river
323 long profiles (Fig. 5). Sixteen rivers had knickpoints, of which eight rivers have two

knickpoints and eight rivers have one knickpoint. Eight rivers are found to be without knickpoints. For comparative analysis, rivers to the northeast and southwest of River 11 are divided into two separate groups representing the two margins of the Qianhe Graben.

The length of the rivers with knickpoints ranges from 54.6 - 160.1 km (Table 1), with the longest river (R11) occurring in the center of Qianhe Graben and the shortest river (R24) on the southern margin of the Qianhe Graben. The total drainage area of these catchments varies between 3.3 and 194.9 km^2. As for the rivers without knickpoints, these have an average length of 91.1 km (Table 2).

Fifteen rivers exhibit slope-break knickpoints (Figs. 5 and 6), while only River 2 has a vertical-step knickpoint. These rivers have a moderate or high k_{sn} value, ranging from 11.0 to 115.0 $m^{0.9}$ (Table 1 and Fig. 6). The average of k_{sn} values downstream of the south and north rivers are 71.1 and 50.5 $m^{0.9}$, respectively, while the average k_{sn} upstream are 41.0 and 27.1 $m^{0.9}$, respectively. Therefore, southern rivers have higher k_{sn} values than northern rivers. River 10 has the highest k_{sn} values, where k_{sn} above and below the knickpoint is 11.0 and 115.0 $m^{0.9}$, respectively (Table 1). The k_{sn} is significantly higher below the knickpoint than above for rivers exhibiting slope-break knickpoints, while the k_{sn} of the river with vertical-step knickpoint is similar above and below the knickpoint (Fig. 6). For example, the k_{sn} above and below the vertical-step

345 knickpoint in River 2 is 16.8 and 34.8 $m^{0.9}$, respectively. While the rivers without
346 knickpoints only have one k_{sn} value, ranging from 30.1 to 80.4 $m^{0.9}$ (Table 2).
347
348 To investigate the change of k_{sn} from above to below the knickpoints, the k_{sn} ratios of
349 knickpoints can be investigated (Fig. 7). There is no significant difference between k_{sn}
350 ratios of most knickpoints, ranging from 0.8 - 10.5. The average k_{sn} ratios of south and
351 north knickpoints are 2.7 and 2.0, respectively. The k_{sn} values for River 9 and River 10
352 exceed 7, may confirm that the high change of slope in the north section of this study
353 area.
354
355 To analyse the vertical distribution of knickpoints, two swath profiles (NN' and SS') with
356 a width of 20 km along the strike and paralleling the QMF and TGF are drawn to
357 compare relief against the knickpoint elevation (Fig. 8a and b). Northern knickpoints
358 range between 1000 - 1400 m in elevation, while southern knickpoints decrease in
359 height from 2300 m to 1100 m southwards. There is an obvious feature that the
360 knickpoints elevation is consistent with the relief (Fig. 8). The knickpoints at the
361 northwestern section of the Qianhe Graben have much higher elevation, while the
362 southeastern section are lower. For example, River 10 has the highest knickpoint at
363 2245 m and the highest relief of 1141 m. The knickpoint elevation against relief in south
364 and north profiles (NN' and SS') are plotted (Fig. 8c and d) and show a stronger linear
365 relationship for the knickpoints on the southern rivers (R^2 = 0.58), than for the northern
366 rivers (R^2 = 0.33).

When the horizontal distribution of knickpoints is considered, slope-break knickpoints are present consistently upstream of faults. Whereas the vertical-step knickpoint in River 2 is located on the trace of the GGF (Fig. 5). Additionally, we observe that the upstream distance of knickpoints from faults is greater when the drainage area is larger (Fig. 9), where $L \sim A^{0.64}$ with an R^2 of 0.6. For example, River 10 has a drainage area of 57.3 km^2 and the upstream distance of the knickpoint from the fault is 13.8 km, while River 24 has a drainage area of 19.0 km^2, but the knickpoint has only migrated 7.8 km. This relationship demonstrates that the distance from faults to knickpoints scale with drainage area in these river systems and the knickpoints propagate upstream as a surrogate of stream discharge, in agreement with previous studies (Boulton et al., 2014; Whittaker and Walker, 2015; Castillo, 2017; Kent et al., 2017).

It is interesting to note that the vertical-step knickpoint of River 2 is located on the GGF, and at the boundary between Cretaceous and Ordovician sandstone (Figs. 1c and 5). As previously discussed, vertical-step knickpoints are not directly related to uplift (Haviv et al., 2010; Kirby and Whipple, 2012) and the potential for knickpoint migration upstream is limited (Harkins et al., 2007; Wang et al., 2015). To investigate the significance of the vertical-step knickpoint, further tributaries around River 2 were obtained (Fig. 10a).

Eight vertical-step knickpoints were located on the GGF (Fig. 10a), and the difference of the k_{sn} above and below vertical-step knickpoints is minor (Fig. 10b), ranging from 26.7 to 49.9 $m^{0.9}$ (Table 3). Interestingly other rivers in Qianhe Graben, such as Rivers 3 to 7, also cross the GGF but do not have the vertical-step knickpoints (Fig. 5). River 2 traverses the change from Cretaceous to Ordovician sandstones and limestones whereas further north Cretaceous sediments are juxtaposed against Neogene sediments of similar rheology (Fig. 1c). Therefore, the lithological strength contrast across the fault is likely the cause of the vertical-step knickpoints, giving a new insight into the location of this fault.

Finally, information on the eight longitudinal profiles without knickpoints was obtained using log(S) curve on SA plot to reveal the uplift rate of these rivers, and applying linear, exponential, logarithmic and power functions to regress the best shape for the long profile (Table 2). As shown in Table 2, log(S) curves on SA plot are convex in River 4, 13 and 15, and the other are linear. The logarithmic function is the best fit to this subset of rivers, where the coefficients of determination (R^2) are > 0.9 (Table 2). The exponent and power function are close to the logarithmic function, and R^2 > 0.79. By contrast, the linear function shows a slightly weaker fit to the data. As discussed in the methodology (Fig. 4b), the shape of logarithmic function shows that in all eight channels incision is high, and the upstream material is transported the downstream accumulation zones.

In summary, the southern margin of the Qianhe Graben has higher relief, elevation, slope, and k_{sn}, while the northern region exhibits lower values for all variables. In addition, the slope-break knickpoints are consistent with being the upstream extent of a transient wave of incision. The reasons for this are explored in the following sections.

5 Discussion

5.1 Why are there knickpoints?

Previous studies have shown that knickpoints can be explained as the result of transient fluvial incision across a region (Wobus et al., 2006; Berlin and Anderson, 2007; Stokes et al., 2008; Kirby and Whipple, 2012; Boulton et al., 2014), where the topographic evolution is related to the interplay between climate, basement lithology and tectonic uplift (Duvall, 2004; Burbank and Anderson, 2011; Kirby and Whipple, 2012; Whittaker and Boulton, 2012; Allen et al., 2013; D'Arcy and Whittaker, 2014; Pérez-Fodich et al., 2014; Martins et al., 2017). In the study area, the knickpoint characteristics are consistent with being the upstream extent of a transient wave of incision, but what caused the landscape perturbation? Here we explore mechanisms for knickpoint development.

Firstly, taking the annual mean precipitation distribution map in 2017 as a sample (Fig. 5b), the annual precipitation varies between 959 and 474 mm but with no clear N-S, or W-E trends. There are also no clear trends shown in the annual precipitation maps of the past 20 years. Additionally, the climatic changes over a longer period were also

considered. Sediment dating data records and the spatial-temporal distribution of vegetation in the Chinese Loess Plateau (Sun et al., 2015, 2017; Xin et al., 2008) suggest that the Holocene climate was dry and cold between 6 and 3 Ka (Wang et al., 2012; Bian et al., 2014). Furthermore, the spatial distribution maps of geomorphic parameters (e.g., hypsometric integral (HI), Stream length-gradient index (SL)) previously used to analyse the relationship between active tectonics and rainfall show no obvious features (Shi et al., 2018; Zhang et al., 2019). Therefore, the knickpoints are unlikely the result precipitation trends, as there is no real variation in rainfall along the Qianhe Graben.

Secondly, knickpoints can be traced along rivers and it is clear that the slope-break knickpoints do not fall on mapped lithological boundaries (Fig. 1c). Interestingly northern knickpoints occur in Cretaceous sandstones, while the southern knickpoints are found across a range of lithologies from Cretaceous sandstones to Early Paleozoic diorite (Fig. 1c and 5). Previous studies have discussed that lithological resistance will not increase the k_{sn} below knickpoints (Snyder et al., 2000; Wobus et al., 2006), suggesting that the presence of most slope-break knickpoints in this area is not caused by the lithological variation.

Finally, is knickpoint formation the result of an increase in footwall uplift related to active faulting? The evidence of slope-break knickpoints, high topographic relief and

gorge formation downstream of knickpoints and that topographic relief scales with knickpoint elevation (Fig. 8) is all consistent with a fault control on knickpoint formation.

In summary, the presence of slope-break knickpoints and other field evidence suggest that knickpoint formation in the study area is the result of transient fluvial response to fault uplift during the late Cenozoic. Furthermore, the vertical-step knickpoints here cannot be ignored in that the lithological strength contrast at fault is likely the cause of these vertical-step knickpoints, giving a new insight into fault location.

5.2 Landscape response to active faults

Previous studies have demonstrated that fault initiation or fault linkage results in an acceleration of uplift, increasing channel steepness as a result of river incision (Tucker and Whipple, 2002; Harkins et al., 2007; Whittaker and Boulton, 2012; Whittaker and Walker, 2015). The horizontal rate of subsequent knickpoint migration is proportion to stream discharge and drainage area (Crosby and Whipple, 2006; Boulton et al., 2014; Whittaker and Walker, 2015; Castillo, 2017), while the vertical rate of knickpoint migration depends on the relative magnitude of fault perturbation or base-level fall (Wobus et al., 2006; Whittaker and Boulton, 2012). Previous studies have also shown that the k_{sn} has a significant positive correlation with rock uplift rate (Snyder et al., 2000; Wobus et al., 2006). However, k_{sn} is not directly transformable into uplift rates (Snyder et al., 2000; Kirby et al., 2003). Using these principals, we can extract more detail on the active faulting of the Qianhe Graben.

Firstly, the vertical component of knickpoint migration was measured as the elevation difference between knickpoints (excluding vertical-step knickpoints) and the likely causative fault (Fig. 11a). The mean and maximum channel elevation difference of this area are ~ 482 and 1136 m, respectively. There is a small decrease from north to south in the elevation difference of the northern knickpoints (Fig. 11b), ranging from 600 - 100 m in height and showing more or less in a linear trend. Southern knickpoints also show a similar trend decreasing from 1150 m in the north to 180 m in the south. The lowest knickpoint height occurs on River 5 at 159 m, which is slightly lower than knickpoints in rivers on either side. Interestingly, this knickpoint is located at the step-over between two segments of TGF (Fig. 5a).

Previous studies have discussed that a fault linkage increases fault uplift rates and forms knickpoints in channels upstream of the linked area as a result of slip acceleration owing to under-displacement of the fault in the linkage zone (Boulton and Whittaker, 2009; Whittaker and Walker, 2015; Kent et al., 2017). In previous examples (i.e., Boulton and Whittaker, 2009; Kent et al., 2017) the knickpoint height along the strike of the fault clearly follows the overall displacement profile on the fault with a number of rivers/knickpoints defining each linked segment. This is not the case for rivers crossing the northern boundary fault of the Qianhe Graben with knickpoint height generally decreasing to the southeast. Nor is there a clear pattern for the rivers crossing the southwestern margin of the graben, although there is a height minima

corresponding to the relay ramp along the TGF but knickpoint elevations are high at either end of the fault array. This pattern of knickpoints indicates that the trend along the southwestern fault is either decreasing to the southeast, or more typical of fault segments but the full length of the faults is longer than previously mapped.

Here we also note that two knickpoints are present on eight of the rivers, where one knickpoint is high in the channel with an upstream catchment area between 1×10^7 m^2 and 1×10^8 m^2 (Fig. 5). Crosby and Whipple (2006) demonstrated that knickpoints migrate upstream until channel incision at low drainage areas prevents efficient incision and results in the knickpoint location at a threshold drainage area, which in the case of the Waipaoa River (New Zealand) is between 1×10^5 m^2 and 1×10^6 m^2. Therefore, our observations suggest that is unlikely that the upper knickpoints are pinned at the threshold drainage area as the drainage areas are at least an order of magnitude greater than recorded by Crosby and Whipple (2006), suggesting that the upper knickpoints are still migrating through the landscape.

As both fault initiation and fault linkage will increase channel steepness and incision causing knickpoint formation and propagation through the river system, it is likely that both signals are being preserved in the landscape of the Qianhe Graben (Tucker and Whipple, 2002; Whittaker and Boulton, 2012; Whittaker and Walker, 2015). Fault initiation occurs prior to fault linkage and therefore, the first incisional wave is marked by the higher knickpoint, while the lower knickpoints may be the result of later fault

519 linkage. Previous studies have shown that the fault segments may evolve without
520 obvious surface connection (soft linkage) or link by breaching the relay zone (hard
521 linkage) (Kim and Sanderson, 2005). There are no relay ramps on north-eastern side
522 of the graben in this study area, although two knickpoints in north-eastern rivers are
523 observed, while the south-western side has a relay ramps along TGF (Fig. 5).
524 Therefore, it is possible that the faults defined the north-eastern side of the graben
525 maybe hard-linked outside of the study area, while the south-western side could be
526 soft-linked across the known relay ramp.
527
528 Interestingly the south-western rivers also have overall higher k_{sn} than the north, which
529 along with higher elevation knickpoints, indicates that the south-western margin is
530 experiencing higher uplift rates. This interpretation is supported by other lines of
531 evidence. Firstly, Song et al. (2001) used paleomagnetic measurements and
532 morphostratigraphy of red bed/clay sequences from pediments to determine that the
533 Liupan Mountain has been uplifting since about 3.8 Ma. Secondly, Chen et al. (2018b)
534 measured the height of highest river terrace (T1 - T5) in the northern of Qianhe Graben,
535 ranging from 8 - 10 m, 20 - 30 m, 60 - 80 m, 130 - 160 m, and 220 - 260 m, suggesting
536 that there is regional uplift with rate of 0.5 - 1.5 mm/yr (Zhang et al., 2019). These
537 results support our observations and suggest that the north-eastern margin of the
538 Qianhe Graben is experiencing lower rates of uplift than the south-western margin.
539

Additionally, in terms of the eight longitudinal profiles without knickpoints, although these rivers are not analyzed in a same way, they are still responding to the regional uplift rate. For example, River 4 does not exhibit knickpoints on the longitudinal profiles but shows a convex log(*S*) form on SA plot (Fig. 6), suggesting that the uplift rate > erosion rate in this location. On the opposite margin, the River 17 shows a linear log(*S*) form on SA plot, indicating that the uplift rate ≈ erosion rate. Therefore, the south-western rivers without knickpoints have likely higher uplift rates than north-eastern rivers as the erosion rate is assumed to be similar in the absence of erosion data. Similar to the rivers exhibiting knickpoints, the k_{sn} is higher for the south-western rivers without knickpoints than north-eastern rivers (Table 2), suggesting that the uplift rate is higher in south-western margin of Qianhe Graben. Although, these results do not give absolute values of uplift rates, these data provide additional evidence into patterns of rock uplift where the rivers without knickpoints are located.

Landscape response time

Previous studies have demonstrated that knickpoint retreat rates act as a pivotal part of the landscape response time, and that the propagation rate depends on the uplift rate of faults and strength of basement rocks in tectonically active settings (Boulton and Whittaker, 2009; Jansen et al., 2011; Whittaker and Boulton, 2012; Allen et al., 2013; Castillo et al., 2013, 2017; Castillo, 2017; Kent et al., 2017). Therefore, investigating the migration of the knickpoints triggered by fault uplift is another way to reveal the landscape response to active faulting.

As shown in Fig. 9, the function ($L \sim A^{0.64}$) demonstrates that the knickpoints follow a common scaling across the study area suggesting that the knickpoints formed at similar times across the graben. Furthermore, the basal loess beds ages can be used to determine the age of river incision as the isochrones of loess sequences can be accurately recognized (Zhang et a., 2019). Based on magnetostratigraphy, previous studies have shown that fault initiation occurred before 1.2 - 1.4 Myr (Chen et al., 2018b; Zhang et al., 2019). Therefore, using the upstream distance from faults to knickpoints and 1.2 - 1.4 Myr as the time of knickpoint formation, the retreat rates of knickpoints was estimated (Fig. 12; Tables 1 and 4). We recognise that there are a number of uncertainties herein regarding the knickpoint formation mechanism, the timing of a) fault initiation and b) fault linkage, and how the terraces ages relate to these events; however, in the absence of other constraints, the 1.2 - 1.4 Myr age range allows us to estimate knickpoint retreat rates for the highest knickpoint in each river (Fig. 12). Furthermore, this timescale is similar to knickpoint ages quoted elsewhere for extensional systems (i.e., Boulton and Whittaker, 2009; Kent et al., 2017).

The retreat rates of knickpoints in Qianhe Graben range from 0.3 to 27.3 mm/yr (Table 4), similar to the Gediz Graben (4.5 - 28.0 mm/yr) (Kent et al., 2017), and the Central Apennines of Italy (1.4 - 10.7 mm/yr) (Whittaker et al., 2007). As some previous studies show (Whittaker and Boulton, 2012; Castillo et al., 2017), the retreat rates of knickpoints increase quickly with the total drainage area above faults. As shown in Fig.

12, southern rivers with knickpoints have higher retreat rates and larger drainage area above knickpoints than in the northern. For example, River 9 has higher knickpoint retreat rate (27.3 mm/yr at 1.2 Myr) and total drainage area (139.1 km^2), while the River 5 has the lowest retreat rate (4.0 mm/yr at 1.2 Myr) and total drainage area (66.3 km^2). Furthermore, knickpoints retreat rates of TGF and QMF decrease from north to south along the strike of fault array, consistent with knickpoint elevation and k_{sn}, further supporting the interpretation that the fault uplift will increase to the northwest and decrease with the loss of stream discharge to southeast. These results above indicate that the higher uplift rates induced the knickpoints to migrate further in the north.

Finally, to compare with other knickpoints in different sites (e.g., Hayakawa and Matsukura, 2003; Bishop et al., 2005; Whittaker et al., 2007; Loget and Van Den Driessche, 2009; Whittaker and Boulton, 2012; Ye et al., 2013; Castillo, 2017; Kent et al., 2017), selecting 1.4 Myr as the minimum age of the fault initiation in Qianhe Graben and all the knickpoints (except for the lower knickpoints) retreat rates against drainage area are shown in Fig. 13. Of these different sites, the knickpoint retreat rates related to Messinian Salinity Crisis (MSC) in the Mediterranean Sea (Loget and Van Den Driessche, 2009) are the fastest (0.25 - 20.00 m/yr), occurred over 0.1 - 1.0 Myr, which induced by base-level fall as a result of sea-level fall. While the retreat rates of Puerto Vallarta in west-central Mexico (Castillo, 2017) are the slowest (0.07 - 0.72 mm/yr), and the age of the rock uplift is 12.5 Kyr, which was caused by base-level fall as a result of faulting.

606

607 Interestingly, published data can be divided into two groups based upon the
608 mechanism of knickpoint formation, where the first group induced by base-level fall as
609 a result of faulting has the higher linear fit (R^2 = 0.80), while linear fit of the second
610 group caused by eustatic sea-level fall is 0.62 (Fig. 13). These robust fits indicate that
611 the fault controlled knickpoints generally have slower retreat rates, than when
612 triggered by sea-level fall, and that fault slip rate likely strongly controls the speed of
613 knickpoint migration (c.f., Boulton and Whittaker, 2009).

614

615 When base-level fall as a result of sea-level fall is considered, the knickpoint retreat
616 rate does not seem to be related to the age of sea-level fall events. By contrast, the
617 retreat rates caused base-level fall as a result of faulting seem to be negatively related
618 to the time of faulting events, indicating that the older faulting events have lower
619 knickpoint retreat rates. Older faulting events having lower retreat rates can be
620 explained as a result of the drainage area decreasing as knickpoints migrate upstream
621 resulting in a loss of erosional efficiency and slowing down knickpoint migration
622 (Crosby and Whipple, 2006; Castillo, 2017).

623

624 However, it is not clear why this is also not true of sea-level fall knickpoints or why the
625 scaling relationship is different depending on the knickpoint trigger mechanism. Ye et
626 al., (2013) suggests that the knickpoint retreat rate on Tahiti may be independent of
627 drainage area as a result of the generally small size of the catchments studied. Yet,

this is not the case for knickpoints studied by Loget and Van Den Driessche (2009) who show the drainage area dependency on knickpoints formed during the MSC. Therefore, the difference in scaling is unlikely the result of drainage area differences. However, it is notable that most sea-level fall knickpoints are described as steep waterfalls that migrate because of plunge-pool erosion (i.e., Ye et al., 2013) as opposed to stream-power dependent erosion along a steep bedrock river. Therefore, we hypothesise that different mechanisms of erosion account for the difference in scaling observed.

5.3 Fault linkage causing knickpoints

As shown previously, we hypothesize that the two segments of TGF faults are currently linked (Fig. 5a and 14a). However, relay breaching faults are not observed leading to some uncertainty in the current fault geometry. Fault linkage and growth are important processes in basin-bounding normal fault systems (Peacock, 2002; Kairanov et al., 2019) where normal fault segments are composed of overlapping segments (Childs et al., 2009; Wang et al., 2018a). Previous studies have addressed that fault growth occurs via increasing fault length and displacement (Walsh and Watterson, 1988; Walsh et al., 2003), where the final fault length will be estimated by the fault's slip history and will grow mainly by displacement accrual (Nicol et al., 2010; Jackson and Rotevatn, 2013; Rotevatn et al., 2018). Additionally, the fault displacement-length model (Wells and Coppersmith, 1994; Soliva and Benedicto, 2004; Kim and Sanderson, 2005; Rotevatn et al., 2018; Wang et al., 2018a), allows individual faults

650 to have finite lengths and thus along-strike strain or displacement variations can be
651 predicted (Nicol et al., 2002; Fossen and Rotevatn, 2016). Therefore, these models of
652 fault scaling can be used to study the character of normal TGF growth and linkage.
653
654 Many researchers have proposed that faults have a constant d_{max}/L ratio for individual
655 fault arrays (Soliva and Benedicto, 2004; Kim and Sanderson, 2005; Schultz et al.,
656 2008; Soliva et al., 2008; Li et al., 2018; Torabi et al., 2019), where the d_{max} and L are
657 the maximum cumulative displacement on a fault and the maximum length of the fault,
658 respectively. The d_{max}/L ratio depends on the tectonic regime and the rate of fault
659 propagation (Peacock and Sanderson, 1996; Kim and Sanderson, 2005).
660
661 As shown in Fig. 14a, two stages are used to describe the patterns of TGF (southern
662 fault) before and after fault linkages. During stage 1, two initially isolated fault
663 segments of TGF are 40.1 and 48.3 km in length, respectively, and propagate towards
664 each other. The displacements of north and southern sections are calculated by the
665 ratio d_{max}/L = 0.04 (Kim et al., 2001), resulting in a displacement of 1.6 and 1.9 *km*,
666 respectively (Fig. 14b). At stage 2, the faults segments interact with each other and
667 may be linked by breaching the relay zone (Fig. 14a). After linkage, fault length will be
668 84.9 *km* (Fig. 14c). The displacement is estimated by the ratio d_{max}/L = 0.025 (Kim and
669 Sanderson, 2005), resulting in a predicted displacement of 2.1 *km* after fault linkage
670 (Fig. 14b). This event will cause slip rates to increase in the center of the fault as a

result of under displacement resulting in a second phase of knickpoint propagation to take place.

This thought experiment is important because it can reveal how normal faults grow and link in the basin, the frequency and magnitude of seismic hazard along the length of a fault array (Cowie and Roberts, 2001; Soliva et al., 2008; Boulton and Whittaker, 2009; Nicol et al., 2010; Kent et al., 2017) and the long-term tectono-stratigraphic development of graben (Gawthorpe and Leeder, 2000; Ge et al., 2018). The seismic hazard of this loess-covered area is not well known. Therefore, it is possible to use the fault displacement-length model and fault surface rupture length to predict the magnitude of potential earthquakes before and after fault linkage. In an earthquake, between one-half and one-third of the total fault length will rupture (Mark, 1977; Kayabali and Akin, 2003). Following Wells and Coppersmith (1994), the magnitude (M_w) can be expressed as follows:

$$Mw = 4.86 + 1.32 \log L \quad (8)$$

Where M_w is moment magnitude L is fault rupture length (in km).

For the northern TGF segment, rupture of one half to one third of the fault would be 13.4 and 20.1 km, while the ruptures of southern segments are 16.1 and 24.2 km, respectively. Before linkage, this could result in earthquakes on the northern and southern faults with predicted M_w of 6.3 - 6.6 and 6.5 - 6.7, respectively. After linkage,

692 the ruptures of one-third to one-half of the TGF are 28.3 and 42.5 km, potentially
693 resulting in an earthquake with predicted M_w of 6.8 - 7.0. As for the QMF in the northern
694 margin, the ruptures of one-third to one-half of the QMF are 21.0 and 31.5 km, and
695 there will be potential earthquake with predicted M_w of 6.6 - 6.8. These results are
696 similar to Cheng et al. (2014) discussed before (M_w > 6.0), and consistent with risk
697 map of this area (Fan et al., 2016). Therefore, even one-third of the fault segment will
698 produce a high magnitude earthquake and increase the risk of the seismic hazard after
699 fault linkage. This new finding not only shows the potential risk of seismic hazards
700 revealed by fault linkage event which previous studies never documented, but also
701 stresses that more attention should be paid to the relationship between earthquake
702 and fault length in this area.
703

704 ## 6 Conclusions

705 To investigate the fault activity in the Qianhe Graben of Southwest margin of Ordos,
706 China, we used patterns of knickpoints in longitudinal profiles to analyse the transient
707 fluvial response to active faulting. Vertical-step knickpoints were identified along the
708 trace of the southern part of the GGF revealing new information on the location of this
709 little known structure. Whilst, slope-break knickpoints were identified across the region
710 and were interpreted as the response to the initiation of the main northern (QMF) and
711 southern graben (TGF) boundary faults at 1.2 - 1.4 Myr. These knickpoints migrate
712 upstream, and the effects of the new tectonic boundary conditions propagate
713 throughout the catchment. Calculated retreat rates of knickpoints in this area are in

714 the range 0.3 - 27.3 mm/yr, and consistent with other studies of fault-driven knickpoint
715 formation. Comparison with other previous studies suggests that knickpoints
716 recession induced by base-level fall as a result of faulting are relatively slower than
717 base-level fall as result of sea-level fall.
718
719 Finally, although further research is required to confirm that the southern TGF fault
720 segments are linked, a displacement-length model is used to study the evolution of
721 two TGF isolated segments, and predict the potential earthquake magnitude before
722 and after fault linkage, resulting in M_w of 6.3 - 6.7 and 6.8 - 7.0, respectively.
723 Demonstrating that the growth and linkage of TGF will increase the magnitude and
724 frequency of the earthquakes and other hazards along this structure. All of these
725 observations derived from geomorphic analysis are powerful tools for the geoscientist
726 as they not only quantify the transient landscape response to active faulting but also
727 provide a new insights into seismic hazards and tectono-stratigraphic development,
728 especially in areas difficult to access. Such insights can be critical for future
729 sustainable environmental development and management in areas vulnerable to
730 seismic and related hazards.
731
732 **Acknowledgements**
733 This work was financially supported by the 1:50, 000 geological mapping in the loess
734 covered region of the map sheets: Caobizhen (I48E008021), Liangting (I48E008022),
735 Zhaoxian (I48E008023), Qianyang (I48E009021), Fengxiang (I48E009022), &

Yaojiagou (I48E009023) in Shaanxi Province, China, under Grant [DD-20160060], and the project of open fund for key laboratory of land and resources degenerate and unused land remediation, under Grant [SXDJ2017-7].

References

Allen, G.H., Barnes, J.B., Pavelsky, T.M., Kirby, E., 2013. Lithologic and tectonic controls on bedrock channel form at the northwest Himalayan front. J. Geophys. Res. Earth Surf. 118, 1806–1825. https://doi.org/10.1002/jgrf.20113

Arrowsmith, J.R., Zielke, O., 2009. Tectonic geomorphology of the San Andreas Fault zone from high resolution topography: An example from the Cholame segment. Geomorphology 113, 70–81. https://doi.org/10.1016/j.geomorph.2009.01.002

Azañón, J.M., Galve, J.P., Pérez-Peña, J. V, Giaconia, F., Carvajal, R., Booth-Rea, G., Jabaloy, A., Vázquez, M., Azor, A., Roldán, F.J., 2015. Relief and drainage evolution during the exhumation of the Sierra Nevada (SE Spain): Is denudation keeping pace with uplift? Tectonophysics 663, 19–32. https://doi.org/10.1016/j.tecto.2015.06.015

Berlin, M.M., Anderson, R.S., 2007. Modeling of knickpoint retreat on the Roan Plateau, western Colorado. J. Geophys. Res. 112. https://doi.org/10.1029/2006jf000553

Bian, H., Pang, J., Huang, C., Zha, X., Gao, P., Wang, X., Li, X., Wang, L., 2014. A comparative study of chemical weathering intensity and element transport features of loess-palaeosol in the upper reaches of Hanjiang and Weihe river valleys, China. Geogr. Res. 33, 654. https://doi.org/10.11821/dlyj201404006

Bishop, P., Hoey, T.B., Jansen, J.D., Artza, I.L., 2005. Knickpoint recession rate and catchment area: the case of uplifted rivers in Eastern Scotland. Earth Surf. Process. Landforms 30, 767–778. https://doi.org/10.1002/esp.1191

762 Boulton, S.J., Stokes, M., 2018. Which DEM is best for analyzing fluvial landscape
763 development in mountainous terrains? Geomorphology 310, 168–187.
764 https://doi.org/10.1016/j.geomorph.2018.03.002
765 Boulton, S.J., Stokes, M., Mather, A.E., 2014. Transient fluvial incision as an indicator
766 of active faulting and Plio-Quaternary uplift of the Moroccan High Atlas.
767 Tectonophysics 633, 16–33. https://doi.org/10.1016/j.tecto.2014.06.032
768 Boulton, S.J., Whittaker, A.C., 2009. Quantifying the slip rates, spatial distribution and
769 evolution of active normal faults from geomorphic analysis: Field examples from
770 an oblique-extensional graben, southern Turkey. Geomorphology 104, 299–316.
771 https://doi.org/10.1016/j.geomorph.2008.09.007
772 Burbank, D.W., Anderson, R.S., 2011. Tectonic Geomorphology: Second Edition,
773 Tectonic Geomorphology: Second Edition.
774 https://doi.org/10.1002/9781444345063
775 Castelltort, S., Goren, L., Willett, S.D., Champagnac, J.-D., Herman, F., Braun, J.,
776 2012. River drainage patterns in the New Zealand Alps primarily controlled by
777 plate tectonic strain. Nat. Geosci. 5, 744–748. https://doi.org/10.1038/ngeo1582
778 Castillo, M., 2017. Landscape evolution of the graben of Puerto Vallarta (west-central
779 Mexico) using the analysis of landforms and stream long profiles. J. South Am.
780 Earth Sci. 73, 10–21. https://doi.org/10.1016/j.jsames.2016.11.002
781 Castillo, M., Bishop, P., Jansen, J.D., 2013. Knickpoint retreat and transient bedrock
782 channel morphology triggered by base-level fall in small bedrock river catchments:
783 The case of the Isle of Jura, Scotland. Geomorphology 180–181, 1–9.
784 https://doi.org/10.1016/j.geomorph.2012.08.023
785 Castillo, M., Ferrari, L., Muñoz-Salinas, E., 2017. Knickpoint retreat and landscape
786 evolution of the Amatlán de Cañas half-graben (northern sector of Jalisco Block,
787 western Mexico). J. South Am. Earth Sci. 77, 108–122.
788 https://doi.org/10.1016/j.jsames.2017.05.003
789 Castillo, M., Muñoz-Salinas, E., Ferrari, L., 2014. Response of a landscape to
790 tectonics using channel steepness indices (ksn) and OSL: A case of study from

791 the Jalisco Block, Western Mexico. Geomorphology 221, 204–214.
792 https://doi.org/10.1016/j.geomorph.2014.06.017
793 Chen, J., Zhang, Z., Li, H., Survey, S.I. of G., 2004. The regional geological survey
794 reports of 1: 250 000 Baoji city. Shaanxi Institute of Geological Survey.
795 Chen, M., Hu, X., Wang, W., 2018a. The cause of high-altitude knickpoints on river
796 longitudinal profiles along the Zoulang Nan Shan. Acta Geogr. Sin. 73, 1702–
797 1713. https://doi.org/10.11821/dlxb201809007
798 Chen, S., Fan, S., Wang, X., Wang, R., Liu, Y., Yang, L., Ning, X., Li, R., Li, S., 2018b.
799 Neotectonic movement in the southern margin of the Ordos Block inferred from
800 the Qianhe River terraces near the north of the Qinghai-Tibet Plateau. Geol. J. 53,
801 274–281. https://doi.org/10.1002/gj.3111
802 Chen, Y.-C., Sung, Q., Chen, C.-N., 2006. Stream-power incision model in non-
803 steady-state mountain ranges: An empirical approach. Chinese Sci. Bull. 51,
804 2789–2794. https://doi.org/10.1007/s11434-006-2194-x
805 Chen, Y.-C., Sung, Q., Cheng, K.-Y., 2003. Along-strike variations of morphotectonic
806 features in the Western Foothills of Taiwan: tectonic implications based on
807 stream-gradient and hypsometric analysis. Geomorphology 56, 109–137.
808 https://doi.org/10.1016/s0169-555x(03)00059-x
809 Cheng, B., Cheng, S., Zhang, G., Zhao, D., 2014. Seismic structure of the Helan–
810 Liupan–Ordos western margin tectonic belt in North-Central China and its
811 geodynamic implications. J. Asian Earth Sci. 87, 141–156.
812 https://doi.org/10.1016/j.jseaes.2014.01.006
813 Cheng, Y., He, C., Rao, G., Yan, B., Lin, A., Hu, J., Yu, Y., Yao, Q., 2018.
814 Geomorphological and structural characterization of the southern Weihe Graben,
815 central China: Implications for fault segmentation. Tectonophysics 722, 11–24.
816 https://doi.org/10.1016/j.tecto.2017.10.024
817 Childs, C., Manzocchi, T., Walsh, J.J., Bonson, C.G., Nicol, A., Schöpfer, M.P.J., 2009.
818 A geometric model of fault zone and fault rock thickness variations. J. Struct. Geol.
819 31, 117–127. https://doi.org/10.1016/j.jsg.2008.08.009

820 Cowie, P.A., Roberts, G.P., 2001. Constraining slip rates and spacings for active
821 normal faults. J. Struct. Geol. 23, 1901–1915. https://doi.org/10.1016/S0191-
822 8141(01)00036-0
823 Crosby, B.T., Whipple, K.X., 2006. Knickpoint initiation and distribution within fluvial
824 networks: 236 waterfalls in the Waipaoa River, North Island, New Zealand.
825 Geomorphology 82, 16–38. https://doi.org/10.1016/j.geomorph.2005.08.023
826 Cyr, A.J., Granger, D.E., Olivetti, V., Molin, P., 2014. Distinguishing between tectonic
827 and lithologic controls on bedrock channel longitudinal profiles using cosmogenic
828 10Be erosion rates and channel steepness index. Geomorphology 209, 27–38.
829 https://doi.org/10.1016/j.geomorph.2013.12.010
830 D'Arcy, M., Whittaker, A.C., 2014. Geomorphic constraints on landscape sensitivity to
831 climate in tectonically active areas. Geomorphology 204, 366–381.
832 https://doi.org/10.1016/j.geomorph.2013.08.019
833 Dong, S., Zhang, P., Zhang, H., Zheng, W., Chen, H., 2017. Drainage Responses to
834 the Activity of the Langshan Range-Front Fault and Tectonic Implications. J. Earth
835 Sci. 29, 193–209. https://doi.org/10.1007/s12583-017-0902-8
836 Duvall, A., 2004. Tectonic and lithologic controls on bedrock channel profiles and
837 processes in coastal California. J. Geophys. Res. 109.
838 https://doi.org/10.1029/2003jf000086
839 Faghih, A., Esmaeilzadeh Soudejani, A., Nourbakhsh, A., Rokni, S., 2015. Tectonic
840 geomorphology of High Zagros Ranges, SW Iran: an initiative towards seismic
841 hazard assessment. Environ. Earth Sci. 74, 3007–3017.
842 https://doi.org/10.1007/s12665-015-4331-9
843 Fan, J., Ma, J., Gan, W., 2003. Movement of Ordos block and alternation of activity
844 along its boundaries. Sci. China Ser. D Earth Sci. 46, 168–180.
845 https://doi.org/10.1360/03dz0013
846 Fan, S.-H., Chen, S.-E., Li, R., Li, S., 2018. Combined effects of the subductions of
847 the Pacific Plate and Indian Plate in Central China in the Cenozoic: Recorded
848 from the Wei River Basin. Geol. J. 53, 266–273. https://doi.org/10.1002/gj.3098

Fan, S., Li, R., Wang, R., 2016. the 1:50,000 geological mapping in the loess‐covered region with the map sheets: Caobizhen (I48E008 021), Liangting (I48E008022), Zhaoxian(I48E008023), Qianyang (I48E009021), Feng xiang (I48E009022), and Yaojiagou (I48E009023) in Shaanxi Province of China. Chang'an University, China.

Farr, T.G., Rosen, P.A., Caro, E., Crippen, R., Duren, R., Hensley, S., Kobrick, M., Paller, M., Rodriguez, E., Roth, L., Seal, D., Shaffer, S., Shimada, J., Umland, J., Werner, M., Oskin, M., Burbank, D., Alsdorf, D., 2007. The Shuttle Radar Topography Mission. Rev. Geophys. 45. https://doi.org/10.1029/2005rg000183

Flint, J.J., 1974. Stream gradient as a function of order, magnitude, and discharge. Water Resour. Res. 10, 969–973. https://doi.org/10.1029/WR010i005p00969

Fossen, H., Rotevatn, A., 2016. Fault linkage and relay structures in extensional settings—A review. Earth-Science Rev. 154, 14–28. https://doi.org/10.1016/j.earscirev.2015.11.014

Gailleton, B., Mudd, S.M., Clubb, F.J., Peifer, D., Hurst, M.D., 2019. A segmentation approach for the reproducible extraction and quantification of knickpoints from river long profiles. Earth Surf. Dyn. 7, 211–230. https://doi.org/10.5194/esurf-7-211-2019

Gawthorpe, R.L., Leeder, M.R., 2000. Tectono-sedimentary evolution of active extensional basins. Basin Res. 12, 195–218. https://doi.org/10.1111/j.1365-2117.2000.00121.x

Ge, Z., Nemec, W., Gawthorpe, R.L., Rotevatn, A., Hansen, E.W.M., 2018. Response of unconfined turbidity current to relay-ramp topography: insights from process-based numerical modelling. Basin Res. 30, 321–343. https://doi.org/10.1111/bre.12255

Giletycz, S., Loget, N., Chang, C.P., Mouthereau, F., 2015. Transient fluvial landscape and preservation of low-relief terrains in an emerging orogen: Example from Hengchun Peninsula, Taiwan. Geomorphology 231, 169–181. https://doi.org/10.1016/j.geomorph.2014.11.026

878 Guo, X., Gao, R., Li, S., Xu, X., Huang, X., Wang, H., Li, W., Zhao, S., Li, X., 2016.
879 Lithospheric architecture and deformation of NE Tibet: New insights on the
880 interplay of regional tectonic processes. Earth Planet. Sci. Lett. 449, 89–95.
881 https://doi.org/10.1016/j.epsl.2016.05.045
882 Hack, J.T., 1973. Stream-profile analysis and stream-gradient index. J. Res. U.S. Geol.
883 Surv. 1, 421–429.
884 Hack, J.T., 1957. Studies of Longitudinal Stream Profiles in Virginia and Maryland.
885 Geol. Surv. Prof. Pap.
886 Han, L., Liu, Z., Ning, Y., Zhao, Z., 2018. Extraction and analysis of geological
887 lineaments combining a DEM and remote sensing images from the northern Baoji
888 loess area. Adv. Sp. Res. 62, 2480–2493.
889 https://doi.org/10.1016/j.asr.2018.07.030
890 Hancock, G.R., Martinez, C., Evans, K.G., Moliere, D.R., 2006. A comparison of SRTM
891 and high-resolution digital elevation models and their use in catchment
892 geomorphology and hydrology: Australian examples. Earth Surf. Process.
893 Landforms 31, 1394–1412. https://doi.org/10.1002/esp.1335
894 Harkins, N., Kirby, E., Heimsath, A., Robinson, R., Reiser, U., 2007. Transient fluvial
895 incision in the headwaters of the Yellow River, northeastern Tibet, China. J.
896 Geophys. Res. 112. https://doi.org/10.1029/2006jf000570
897 Haviv, I., Enzel, Y., Whipple, K.X., Zilberman, E., Matmon, A., Stone, J., Fifield, K.L.,
898 2010. Evolution of vertical knickpoints (waterfalls) with resistant caprock: Insights
899 from numerical modeling. J. Geophys. Res. 115.
900 https://doi.org/10.1029/2008jf001187
901 Hayakawa, Y., Matsukura, Y., 2003. Recession rates of waterfalls in Boso Peninsula,
902 Japan, and a predictive equation. Earth Surf. Process. Landforms 28, 675–684.
903 https://doi.org/10.1002/esp.519
904 Hergarten, S., Robl, J., Stüwe, K., 2016. Tectonic geomorphology at small catchment
905 sizes – extensions of the stream-power approach and the
906 <i>χ</i> method. Earth Surf. Dyn. 4, 1–9.
907 https://doi.org/10.5194/esurf-4-1-2016

Hou, J.-J., Han, M.-K., Chai, B.-L., Han, H.-Y., 1998. Geomorphological observations of active faults in the epicentral region of the Huaxian large earthquake in 1556 in Shaanxi Province, China. J. Struct. Geol. 20, 549–557. https://doi.org/10.1016/S0191-8141(97)00112-0

Howard, A.D., Dietrich, W.E., Seidl, M.A., 1994. Modeling Fluvial Erosion on Regional to Continental Scales. J. Geophys. Res. Solid Earth 99, 13971–13986. https://doi.org/10.1029/94jb00744

Howard, A.D., Kerby, G., 1983. Channel Changes in Badlands. Geol. Soc. Am. Bull. 94, 739–752. https://doi.org/10.1130/0016-7606(1983)942.0.CO;2

Jackson, C.A.L., Rotevatn, A., 2013. 3D seismic analysis of the structure and evolution of a salt-influenced normal fault zone: A test of competing fault growth models. J. Struct. Geol. 54, 215–234. https://doi.org/10.1016/j.jsg.2013.06.012

Jansen, J.D., Fabel, D., Bishop, P., Xu, S., Schnabel, C., Codilean, A.T., 2011. Does decreasing paraglacial sediment supply slow knickpoint retreat? Geology 39, 543–546. https://doi.org/10.1130/G32018.1

Jiang, W., Han, Z., Zhang, J., Jiao, Q., 2016. Stream profile analysis, tectonic geomorphology and neotectonic activity of the Damxung-Yangbajain rift in the south Tibetan Plateau. Earth Surf. Process. Landforms 41, 1312–1326. https://doi.org/10.1002/esp.3899

Kairanov, B., Marín, D., Escalona, A., Cardozo, N., 2019. Growth and linkage of a basin-bounding fault system: Insights from the Early Cretaceous evolution of the northern Polhem Subplatform, SW Barents Sea. J. Struct. Geol. https://doi.org/10.1016/j.jsg.2019.04.014

Kale, V.S., Sengupta, S., Achyuthan, H., Jaiswal, M.K., 2014. Tectonic controls upon Kaveri River drainage, cratonic Peninsular India: Inferences from longitudinal profiles, morphotectonic indices, hanging valleys and fluvial records. Geomorphology 227, 153–165. https://doi.org/10.1016/j.geomorph.2013.07.027

Kayabali, K., Akin, M., 2003. Seismic hazard map of Turkey using the deterministic approach. Eng. Geol. 69, 127–137. https://doi.org/10.1016/s0013-7952(02)00272-7

Kent, E., Boulton, S.J., Stewart, I.S., Whittaker, A.C., Alçiçek, M.C., 2016. Geomorphic and geological constraints on the active normal faulting of the Gediz (Alaşehir) Graben, Western Turkey. J. Geol. Soc. London. 173, 666–678. https://doi.org/10.1144/jgs2015-121

Kent, E., Boulton, S.J., Whittaker, A.C., Stewart, I.S., Cihat Alçiçek, M., 2017. Normal fault growth and linkage in the Gediz (Alaşehir) Graben, Western Turkey, revealed by transient river long-profiles and slope-break knickpoints. Earth Surf. Process. Landforms 42, 836–852. https://doi.org/10.1002/esp.4049

Kim, Y.-S., Andrews, J.R., Sanderson, D.J., 2001. Reactivated strike–slip faults: examples from north Cornwall, UK. Tectonophysics 340, 173–194. https://doi.org/10.1016/S0040-1951(01)00146-9

Kim, Y.-S., Sanderson, D.J., 2005. The relationship between displacement and length of faults: a review. Earth-Science Rev. 68, 317–334. https://doi.org/10.1016/j.earscirev.2004.06.003

Kirby, E., Ouimet, W., 2011. Tectonic geomorphology along the eastern margin of Tibet: insights into the pattern and processes of active deformation adjacent to the Sichuan Basin. Geol. Soc. London, Spec. Publ. 353, 165–188. https://doi.org/10.1144/sp353.9

Kirby, E., Whipple, K., 2001. Quantifying differential rock-uplift rates via stream profile analysis. Geology 29, 415–418. https://doi.org/10.1130/0091-7613(2001)029<0415:qdrurv>2.0.co;2

Kirby, E., Whipple, K.X., 2012. Expression of active tectonics in erosional landscapes. J. Struct. Geol. 44, 54–75. https://doi.org/10.1016/j.jsg.2012.07.009

Kirby, E., Whipple, K.X., Tang, W., Chen, Z., 2003. Distribution of active rock uplift along the eastern margin of the Tibetan Plateau: Inferences from bedrock channel longitudinal profiles. J. Geophys. Res. Solid Earth 108. https://doi.org/10.1029/2001jb000861

Li, B., Ling, Z., Zhang, J., Chen, J., Ni, Y., Liu, C., 2018. Displacement-length ratios and contractional strains of lunar wrinkle ridges in Mare Serenitatis and Mare

967 Tranquillitatis. J. Struct. Geol. 109, 27–37.
968 https://doi.org/10.1016/j.jsg.2018.01.003
969 Li, J., 1991. The environmental effects of the uplift of the Qinghai-Xizang Plateau. Quat.
970 Sci. Rev. 10, 479–483. https://doi.org/10.1016/0277-3791(91)90041-R
971 Li, L., Xu, G., Hu, J., Yu, X., 2012. An analysis of relative active tectonics based on
972 DEM. Geol. China 39, 595-604 (in Chinese with English abstract).
973 Li, W., Dong, Y., Guo, A., Liu, X., Zhou, D., 2013. Chronology and tectonic significance
974 of Cenozoic faults in the Liupanshan Arcuate Tectonic Belt at the northeastern
975 margin of the Qinghai–Tibet Plateau. J. Asian Earth Sci. 73, 103–113.
976 https://doi.org/10.1016/j.jseaes.2013.04.026
977 Liang, M., Wang, Z., Zhou, S., Zong, K., Hu, Z., 2014. The provenance of Gansu Group
978 in Longxi region and implications for tectonics and paleoclimate. Sci. China Earth
979 Sci. 57, 1221–1228. https://doi.org/10.1007/s11430-013-4787-y
980 Lin, A., Rao, G., Yan, B., 2015. Flexural fold structures and active faults in the
981 northern–western Weihe Graben, central China. J. Asian Earth Sci. 114, 226–241.
982 https://doi.org/10.1016/j.jseaes.2015.04.012
983 Lin, X., Chen, H., Wyrwoll, K.-H., Batt, G.E., Liao, L., Xiao, J., 2011. The Uplift History
984 of the Haiyuan-Liupan Shan Region Northeast of the Present Tibetan Plateau:
985 Integrated Constraint from Stratigraphy and Thermochronology. J. Geol. 119,
986 372–393. https://doi.org/10.1086/660190
987 Loget, N., Van Den Driessche, J., 2009. Wave train model for knickpoint migration.
988 Geomorphology 106, 376–382. https://doi.org/10.1016/j.geomorph.2008.10.017
989 Mark, R.K., 1977. Application of linear statistical models of earthquake magnitude
990 versus fault length in estimating maximum expectable earthquakes. Geology 5,
991 464–466. https://doi.org/10.1130/0091-7613(1977)5<464:aolsmo>2.0.co;2
992 Martins, A.A., Cabral, J., Cunha, P.P., Stokes, M., Borges, J., Caldeira, B., Martins,
993 A.C., 2017. Tectonic and lithological controls on fluvial landscape development in
994 central-eastern Portugal: Insights from long profile tributary stream analyses.
995 Geomorphology 276, 144–163. https://doi.org/10.1016/j.geomorph.2016.10.012

Matoš, B., Pérez-Peña, J.V., Tomljenović, B., 2016. Landscape response to recent tectonic deformation in the SW Pannonian Basin: Evidence from DEM-based morphometric analysis of the Bilogora Mt. area, NE Croatia. Geomorphology 263, 132–155. https://doi.org/10.1016/j.geomorph.2016.03.020

Nexer, M., Authemayou, C., Schildgen, T., Hantoro, W.S., Molliex, S., Delcaillau, B., Pedoja, K., Husson, L., Regard, V., 2015. Evaluation of morphometric proxies for uplift on sequences of coral reef terraces: A case study from Sumba Island (Indonesia). Geomorphology 241, 145–159. https://doi.org/10.1016/j.geomorph.2015.03.036

Nicol, A., Gillespie, P.A., Childs, C., Walsh, J.J., 2002. Relay zones between mesoscopic thrust faults in layered sedimentary sequences. J. Struct. Geol. 24, 709–727. https://doi.org/10.1016/S0191-8141(01)00113-4

Nicol, A., Walsh, J.J., Villamor, P., Seebeck, H., Berryman, K.R., 2010. Normal fault interactions, paleoearthquakes and growth in an active rift. J. Struct. Geol. 32, 1101–1113. https://doi.org/10.1016/j.jsg.2010.06.018

Ohmori, H., 1991. Change in the Mathematical Function Type Describing the Longitudinal Profile of a River through an Evolutionary Process. J. Geol. 99, 97–110. https://doi.org/10.1086/629476

Olivetti, V., Cyr, A.J., Molin, P., Faccenna, C., Granger, D.E., 2012. Uplift history of the Sila Massif, southern Italy, deciphered from cosmogenic10Be erosion rates and river longitudinal profile analysis. Tectonics 31, n/a-n/a. https://doi.org/10.1029/2011tc003037

Owen, L.A., D. Richardson, N. Castree, M. F. Goodchild, A. Kobayashi, Marston, R.A., 2017. Tectonic Geomorphology, in: International Encyclopedia of Geography. https://doi.org/10.1002/9781118786352.wbieg0606

Ozkaymak, Ç., Sözbilir, H., 2012. Tectonic geomorphology of the Spildağı High Ranges, western Anatolia. Geomorphology 173–174, 128–140. https://doi.org/10.1016/j.geomorph.2012.06.003

1024 Peacock, D.C.P., 2002. Propagation, interaction and linkage in normal fault systems.
1025 Earth-Science Rev. 58, 121–142. https://doi.org/10.1016/S0012-8252(01)00085-
1026 X
1027 Peacock, D.C.P., Sanderson, D.J., 1996. Effects of propagation rate on displacement
1028 variations along faults. J. Struct. Geol. 18, 311–320.
1029 https://doi.org/10.1016/S0191-8141(96)80052-6
1030 Pérez-Fodich, A., Reich, M., Álvarez, F., Snyder, G.T., Schoenberg, R., Vargas, G.,
1031 Muramatsu, Y., Fehn, U., 2014. Climate change and tectonic uplift triggered the
1032 formation of the Atacama Desert's giant nitrate deposits. Geology 42, 251–254.
1033 https://doi.org/10.1130/g34969.1
1034 Rãdoane, M., Rãdoane, N., Dumitriu, D., 2003. Geomorphological evolution of
1035 longitudinal river profiles in the Carpathians. Geomorphology 50, 293–306.
1036 https://doi.org/10.1016/s0169-555x(02)00194-0
1037 Rao, G., Cheng, Y., Lin, A., Yan, B., 2017. Relationship between landslides and active
1038 normal faulting in the epicentral area of the AD 1556 M~8.5 Huaxian Earthquake,
1039 SE Weihe Graben (Central China). J. Earth Sci. 28, 545–554.
1040 https://doi.org/10.1007/s12583-017-0900-z
1041 Regalla, C., Kirby, E., Fisher, D., Bierman, P., 2013. Active forearc shortening in
1042 Tohoku, Japan: Constraints on fault geometry from erosion rates and fluvial
1043 longitudinal profiles. Geomorphology 195, 84–98.
1044 https://doi.org/10.1016/j.geomorph.2013.04.029
1045 Ren, Z., Cui, J., Ke, G., Tao, T., Cao, Z., 2015. Fission-track analysis of uplift times
1046 and processes of the Weibei Uplift in the Ordos Basin. Chinese Sci. Bull. 60, 1298
1047 (in Chinese with English abstract). https://doi.org/10.1360/N972014-00617
1048 Robustelli, G., 2019. Geomorphic constraints on uplift history in the Aspromonte
1049 Massif, southern Italy. Geomorphology 327, 319–337.
1050 https://doi.org/10.1016/j.geomorph.2018.11.011
1051 Rossi, M.W., Quigley, M.C., Fletcher, J.M., Whipple, K.X., Díaz-Torres, J.J., Seiler, C.,
1052 Fifield, L.K., Heimsath, A.M., 2017. Along-strike variation in catchment
1053 morphology and cosmogenic denudation rates reveal the pattern and history of

1054 footwall uplift, Main Gulf Escarpment, Baja California. Geol. Soc. Am. Bull. 129,
1055 837–854. https://doi.org/10.1130/b31373.1
1056 Rotevatn, A., Jackson, C.A.L., Tvedt, A.B.M., Bell, R.E., Blækkan, I., 2018. How do
1057 normal faults grow? J. Struct. Geol. https://doi.org/10.1016/j.jsg.2018.08.005
1058 Schanz, S.A., Montgomery, D.R., 2016. Lithologic controls on valley width and strath
1059 terrace formation. Geomorphology 258, 58–68.
1060 https://doi.org/10.1016/j.geomorph.2016.01.015
1061 Scherler, D., DiBiase, R.A., Fisher, G.B., Avouac, J.-P., 2017. Testing monsoonal
1062 controls on bedrock river incision in the Himalaya and Eastern Tibet with a
1063 stochastic-threshold stream power model. J. Geophys. Res. Earth Surf. 122,
1064 1389–1429. https://doi.org/10.1002/2016JF004011
1065 Schultz, R.A., Soliva, R., Fossen, H., Okubo, C.H., Reeves, D.M., 2008. Dependence
1066 of displacement–length scaling relations for fractures and deformation bands on
1067 the volumetric changes across them. J. Struct. Geol. 30, 1405–1411.
1068 https://doi.org/10.1016/j.jsg.2008.08.001
1069 Sembroni, A., Molin, P., 2018. Long-term drainage system evolution in the Wabe
1070 Shebele River basin (SE Ethiopia - SW Somalia). Geomorphology 320, 45–63.
1071 https://doi.org/10.1016/j.geomorph.2018.08.001
1072 Shi, W., 2011. The analysis of the developmentcharacteristicandactivity aboutfault
1073 zone of Longxian-Baoji. Chang'an University, Xi'an.
1074 Snyder, N.P., Whipple, K.X., Tucker, G.E., Merritts, D.J., 2000. Landscape response
1075 to tectonic forcing: Digital elevation model analysis of stream profiles in the
1076 Mendocino triple junction region, northern California. Geol. Soc. Am. Bull. 112,
1077 1250–1263. https://doi.org/10.1130/0016-
1078 7606(2000)112<1250:LRTTFD>2.0.CO;2
1079 Soliva, R., Benedicto, A., 2004. A linkage criterion for segmented normal faults. J.
1080 Struct. Geol. 26, 2251–2267. https://doi.org/10.1016/j.jsg.2004.06.008
1081 Soliva, R., Benedicto, A., Schultz, R.A., Maerten, L., Micarelli, L., 2008. Displacement
1082 and interaction of normal fault segments branched at depth: Implications for fault

growth and potential earthquake rupture size. J. Struct. Geol. 30, 1288–1299. https://doi.org/10.1016/j.jsg.2008.07.005

Song, Y., Fang, X., Li, J., An, Z., Miao, X., 2001. The Late Cenozoic uplift of the Liupan Shan, China. Sci. China Ser. D Earth Sci. 44, 176–184. https://doi.org/10.1007/BF02911985

Stokes, M., Mather, A.E., Belfoul, A., Farik, F., 2008. Active and passive tectonic controls for transverse drainage and river gorge development in a collisional mountain belt (Dades Gorges, High Atlas Mountains, Morocco). Geomorphology 102, 2–20. https://doi.org/10.1016/j.geomorph.2007.06.015

Sun, A., Guo, Z., Wu, H., Li, Q., Yu, Y., Luo, Y., Jiang, W., Li, X., 2017. Reconstruction of the vegetation distribution of different topographic units of the Chinese Loess Plateau during the Holocene. Quat. Sci. Rev. https://doi.org/10.1016/j.quascirev.2017.08.006

Sun, J., 2005. Long-term fluvial archives in the Fen Wei Graben, central China, and their bearing on the tectonic history of the India?Asia collision system during the Quaternary. Quat. Sci. Rev. 24, 1279–1286. https://doi.org/10.1016/j.quascirev.2004.08.018

Sun, W., Song, X., Mu, X., Gao, P., Wang, F., Zhao, G., 2015. Spatiotemporal vegetation cover variations associated with climate change and ecological restoration in the Loess Plateau. Agric. For. Meteorol. https://doi.org/10.1016/j.agrformet.2015.05.002

Tepe, Ç., Sözbilir, H., 2017. Tectonic geomorphology of the Kemalpaşa Basin and surrounding horsts, southwestern part of the Gediz Graben, Western Anatolia. Geodin. Acta 29, 70–90. https://doi.org/10.1080/09853111.2017.1317191

Topal, S., Keller, E., Bufe, A., Koçyiğit, A., 2016. Tectonic geomorphology of a large normal fault: Akşehir fault, SW Turkey. Geomorphology 259, 55–69. https://doi.org/10.1016/j.geomorph.2016.01.014

Torabi, A., Alaei, B., Libak, A., 2019. Normal fault 3D geometry and displacement revisited: Insights from faults in the Norwegian Barents Sea. Mar. Pet. Geol. 99, 135–155. https://doi.org/10.1016/j.marpetgeo.2018.09.032

Tucker, G.E., Whipple, K.X., 2002. Topographic outcomes predicted by stream erosion models: Sensitivity analysis and intermodel comparison. J. Geophys. Res. Solid Earth 107, ETG 1-1-ETG 1-16. https://doi.org/10.1029/2001jb000162

Walsh, J.J., Bailey, W.R., Childs, C., Nicol, A., Bonson, C.G., 2003. Formation of segmented normal faults: a 3-D perspective. J. Struct. Geol. 25, 1251–1262. https://doi.org/10.1016/S0191-8141(02)00161-X

Walsh, J.J., Watterson, J., 1988. Analysis of the relationship between displacements and dimensions of faults. J. Struct. Geol. 10, 239–247. https://doi.org/10.1016/0191-8141(88)90057-0

Wang, H., Huang, C., Zhou, Y., Pang, J., Zha, X., Gu, H., Zhou, L., 2012. OSL dating of the Holocene paleoflood events on the Qianhe River in the Guanzhong Basin, China. Sci. Sin. Terrae 42, 390–401. https://doi.org/10.1360/zd-2012-42-3-390

Wang, H.B., Zhou, B., Wu, S.R., Shi, J.S., Li, B., 2011. Characteristic analysis of large-scale loess landslides: a case study in Baoji City of Loess Plateau of Northwest China. Hazards Earth Syst. Sci 11, 1829–1837. https://doi.org/10.5194/nhess-11-1829-2011

Wang, H.X., Fu, X.F., Liu, S.R., Chu, R., Liu, B., Shi, P.P., 2018. Quantitative discrimination of normal fault segment growth and its geological significance: example from the Tanan Depression, Tamtsag Basin, Mongolia. Aust. J. Earth Sci. 65, 711–725. https://doi.org/10.1080/08120099.2018.1462850

Wang, N., Han, Z., Li, X., Chen, G., Wang, X., Lu, H., 2015. Tectonic uplift of Mt. Lushan indicated by the steepness indices of the river longitudinal profiles. Acta Gepgraphica Sin. 70, 1516–1525. https://doi.org/10.11821/dlxb201509013

Wang, S., Jiang, F., Zhang, S., Liu, L., Zhu, L., 2017. Present Vertical Deformation and Tectonic Activity in Liupanshan and Its Adjacent Areas. J. Geod. Geodyn. 37, 16–21. https://doi.org/10.14075/j.jgg.2017.01.004

Wang, Y., Zheng, D., Pang, J., Zhang, H., Wang, W., Yu, J., Zhang, Z., Zheng, W., Zhang, P., Li, Y., 2018. Using slope-area and apatite fission track analysis to decipher the rock uplift pattern of the Yumu Shan: New insights into the growth of

1142 the NE Tibetan Plateau. Geomorphology 308, 118–128.
1143 https://doi.org/10.1016/j.geomorph.2018.02.006
1144 Wells, D.L., Coppersmith, K.J., 1994. New empirical relationships among magnitude,
1145 rupture length, rupture width, rupture area, and surface displacement. Bull.
1146 Seismol. Soc. Am. 84, 974–1002.
1147 Whipple, K., Meade, B., 2006. Orogen response to changes in climatic and tectonic
1148 forcing. Earth Planet. Sci. Lett. 243, 218–228.
1149 https://doi.org/10.1016/j.epsl.2005.12.022
1150 Whipple, K., Wobus, C., Crosby, B., Kirby, E., Sheehan, D., 2007. New Tools for
1151 Quantitative Geomorphology: Extraction and Interpretation of Stream Profiles
1152 from Digital Topographic Data, in: GSA Annual Meeting. NSF Geomorphology
1153 and Land Use Dynamics, Boulder, CO.
1154 Whipple, K.X., 2009. The influence of climate on the tectonic evolution of mountain
1155 belts. Nat. Geosci. 2, 97–104. https://doi.org/10.1038/ngeo413
1156 Whipple, K.X., 2004. Bedrock rivers and the geomorpjology of active orogens. Annu.
1157 Rev. Earth Planet. Sci. 32, 151.
1158 https://doi.org/10.1146/annurev.earth.32.101802.120356
1159 Whipple, K.X., 2002. Implications of sediment-flux-dependent river incision models for
1160 landscape evolution. J. Geophys. Res. 107.
1161 https://doi.org/10.1029/2000jb000044
1162 Whipple, K.X., DiBiase, R.A., Crosby, B.T., 2013. 9.28 Bedrock Rivers. Treatise
1163 Geomorphol. 550–573. https://doi.org/10.1016/B978-0-12-374739-6.00254-2
1164 Whipple, K.X., Tucker, G.E., 1999. Dynamics of the stream-power river incision model:
1165 Implications for height limits of mountain ranges, landscape response timescales,
1166 and research needs. J. Geophys. Res. Solid Earth 104, 17661–17674.
1167 https://doi.org/doi:10.1029/1999JB900120
1168 Whittaker, A.C., 2012. How do landscapes record tectonics and climate? Lithosphere
1169 4, 160–164. https://doi.org/10.1130/rf.l003.1

1170 Whittaker, A.C., Attal, M., Cowie, P.A., Tucker, G.E., Roberts, G., 2008. Decoding
1171 temporal and spatial patterns of fault uplift using transient river long profiles.
1172 Geomorphology 100, 506–526. https://doi.org/10.1016/j.geomorph.2008.01.018
1173 Whittaker, A.C., Boulton, S.J., 2012. Tectonic and climatic controls on knickpoint
1174 retreat rates and landscape response times. J. Geophys. Res. Earth Surf. 117,
1175 F02024. https://doi.org/10.1029/2011jf002157
1176 Whittaker, A.C., Cowie, P.A., Attal, M., Tucker, G.E., Roberts, G.P., 2007. Contrasting
1177 transient and steady-state rivers crossing active normal faults: new field
1178 observations from the Central Apennines, Italy. Basin Res. 19, 529–556.
1179 https://doi.org/10.1111/j.1365-2117.2007.00337.x
1180 Whittaker, A.C., Walker, A.S., 2015. Geomorphic constraints on fault throw rates and
1181 linkage times: Examples from the Northern Gulf of Evia, Greece. J. Geophys. Res.
1182 Earth Surf. 120, 137–158. https://doi.org/10.1002/2014jf003318
1183 Wobus, C.W., Crosby, B.T., Whipple, K.X., 2006. Hanging valleys in fluvial systems:
1184 Controls on occurrence and implications for landscape evolution. J. Geophys. Res.
1185 111. https://doi.org/10.1029/2005jf000406
1186 Xin, Z., Xu, J., Zheng, W., 2008. Spatiotemporal variations of vegetation cover on the
1187 Chinese Loess Plateau (1981–2006): Impacts of climate changes and human
1188 activities. Sci. China Ser. D Earth Sci. 51, 67–78. https://doi.org/10.1007/s11430-
1189 007-0137-2
1190 Xue, L., Alemu, T., Gani, N.D., Abdelsalam, M.G., 2018. Spatial and temporal variation
1191 of tectonic uplift in the southeastern Ethiopian Plateau from morphotectonic
1192 analysis. Geomorphology 309, 98–111.
1193 https://doi.org/10.1016/j.geomorph.2018.02.025
1194 Yan, Z., Zhang, H., Fan, X., Du, X., 2015. Geomorphic indices of rivers and drainage
1195 in China’s Longmen Shan Fault zone and their implications for regional tectonic
1196 activity. Geodin. Acta 27, 48–59. https://doi.org/10.1080/09853111.2014.979533
1197 Ye, F.-Y., Barriot, J.-P., Carretier, S., 2013. Initiation and recession of the fluvial
1198 knickpoints of the Island of Tahiti (French Polynesia). Geomorphology 186, 162–
1199 173. https://doi.org/10.1016/j.geomorph.2012.12.031

Zahra, T., Paudel, U., Hayakawa, Y.S., Oguchi, T., 2017. Knickzone Extraction Tool (KET) – A new ArcGIS toolset for automatic extraction of knickzones from a DEM based on multi-scale stream gradients. Open Geosci. 9. https://doi.org/10.1515/geo-2017-0006

Zhang, T., Fan, S., Chen, S., Li, S., Lu, Y., 2019. Geomorphic evolution and neotectonics of the Qianhe River Basin on the southwest margin of the Ordos Block, North China. J. Asian Earth Sci. 176, 184–195. https://doi.org/10.1016/j.jseaes.2019.02.020

Figures and Tables

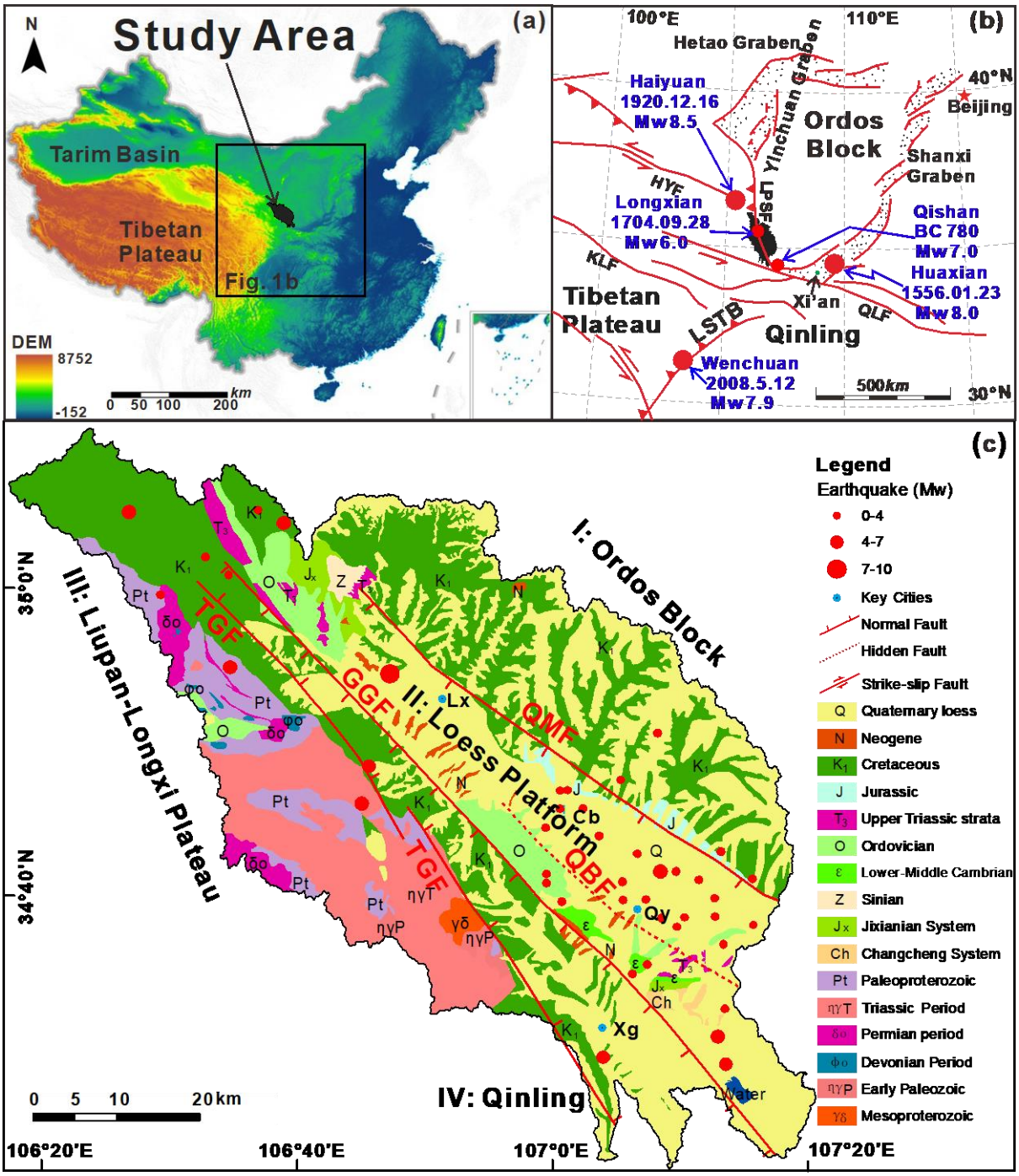

Fig. 1. Simplified regional geological map of Qianhe Basin. (a) map of China, data from http://www.dsac.cn/; (b) map of the regional geological background, adapted from (Rao et al., 2017; Cheng et al., 2018; Han et al., 2018), with earthquake data from (Cheng et al., 2014; Fan et al., 2016, 2018). The red lines are faults in central China: QLF: Qinling Fault; HYF: Haiyuan Fault; KLF: Kunlun Fault; LPSF: Liupanshan Fault; LSTB: Longmen Shan Thrust Belt; (c) The geological map modified from (Chen et al., 2004), showing the main lithologies and the significant regional faults. The four red NW faults are the target fault of this research, Qianhe Basin fault zone. QMF: Qishan-Mazhao Fault; QBF: Qianyang-Biaojiao Fault; GGF: Guguan-Guozhen Fault; TGF: Taoyuan-Guichuansi Fault. Key

cities: Lx, Longxian; Cb, Caobi; Qy, Qianyang; Xg, Xiangong. I: Uplift region of southwestern Ordos's margin; II: Differential descent area of Weihe Basin; III: Differential uplift region of Liupan-Longshan; IV: Qinling uplift area.

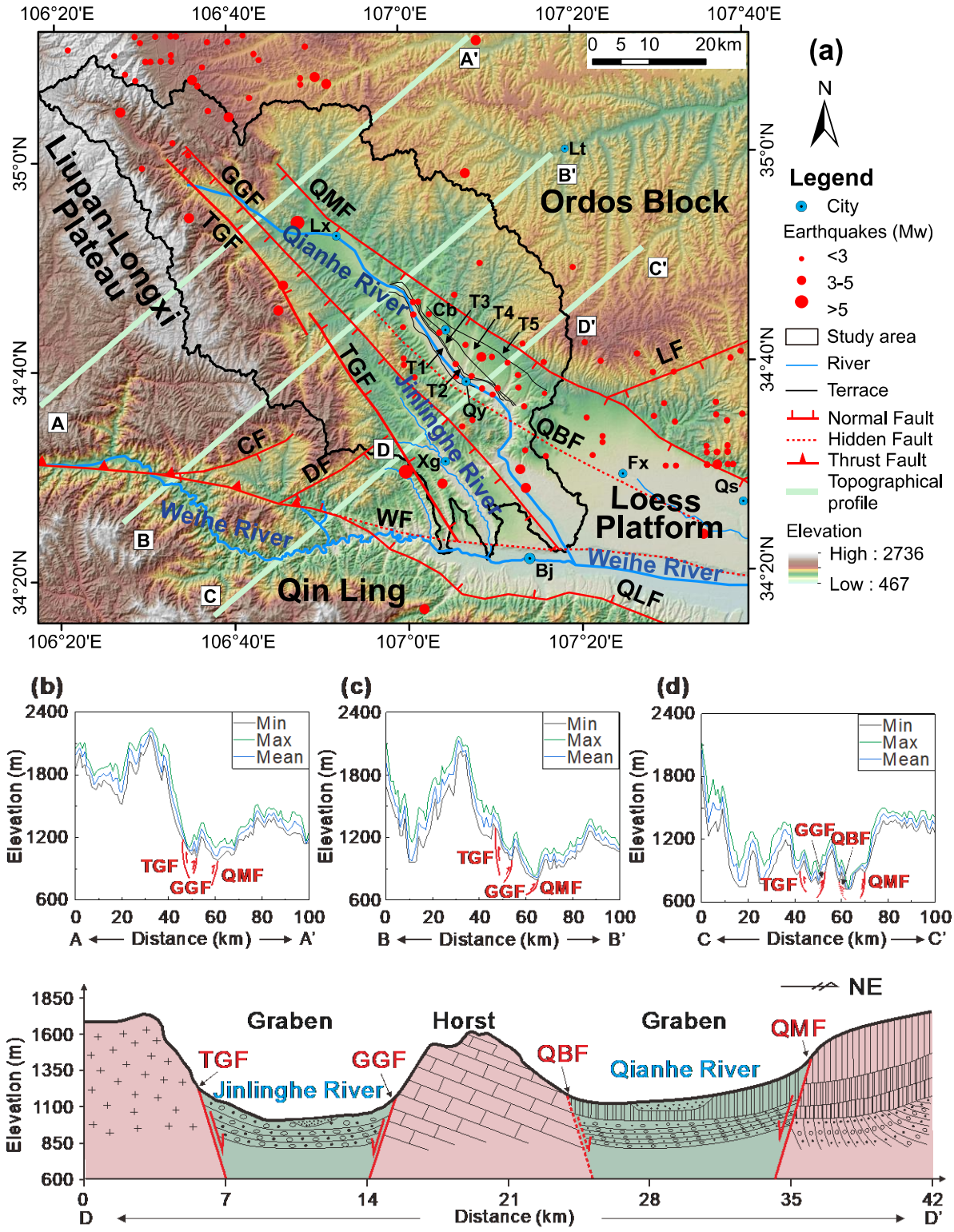

Fig. 2. Geomorphology of the study area. (a) SRTM (1 arc-second, NASA/USGS) was used as the digital elevation model of the Qianhe fault zone, the black terrace lines on the north side of Qianhe modified from (Chen et al., 2018b). Key cities: Lt, Liangting; Cb, Caobi; Qy, Qianyang; Qs, Qishan; Bj, Baoji; Fx, Fengxiang. LF, Linyou Fault; CF, Chishazhen Fault; DF, Duijiashan Fault; QLF, Qinling Fault; WF, Weihe Fault. (b) ~ (d) The topographical profiles of AA', BB', CC', respectively. (e) Tectonic framework modified from Shi (2011).

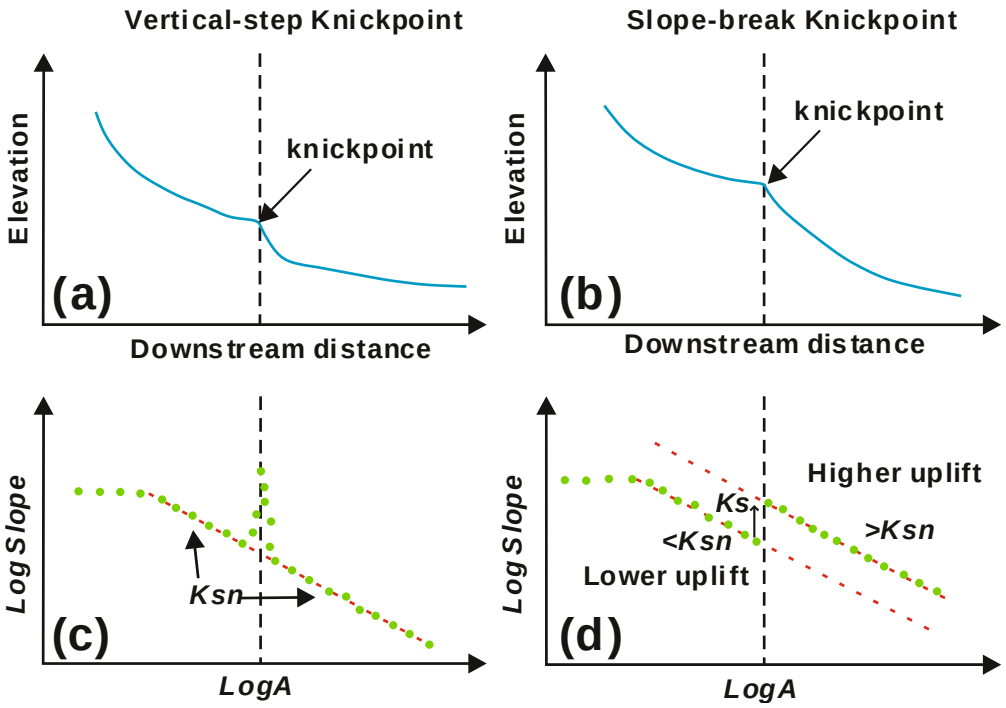

Fig. 3. Knickpoints patterns in terms of river longitudinal profile and log-log slope-area plot. Both morphologies may represent the fluvial response to active faults, modified from Kirby and Whipple (2012).

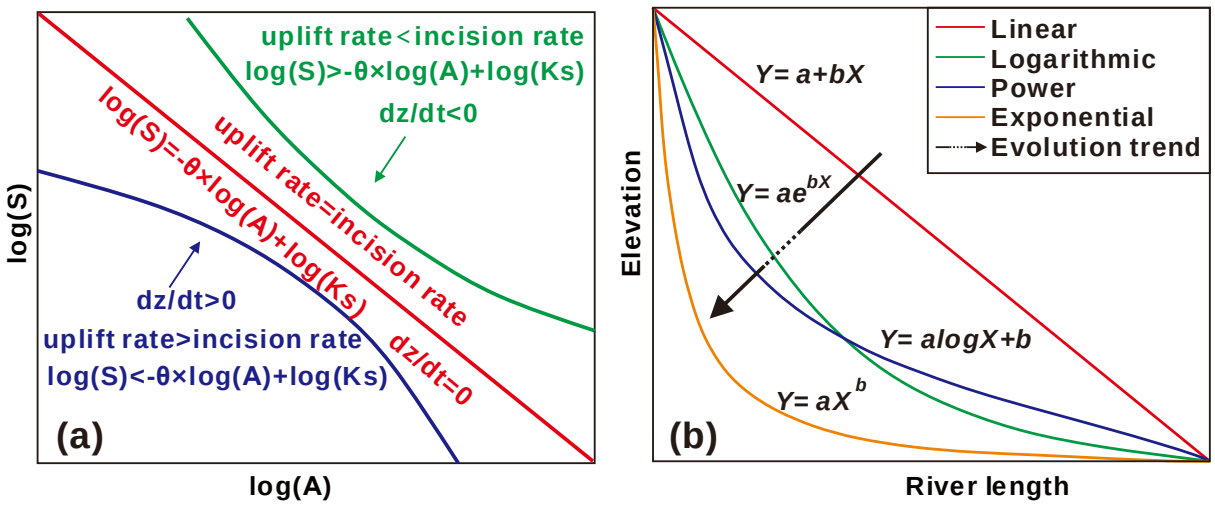

Fig. 4. (a) Standard logarithmic S-A plot of stream-power incision model, modified from (Chen et al., 2006); (b) Fit to the river profile by mathematic models. Where *Y* is elevation; *X* is the length of the river, *a*, *b* are coefficients independently determined for each profile, modified from Dong et al. (2017).

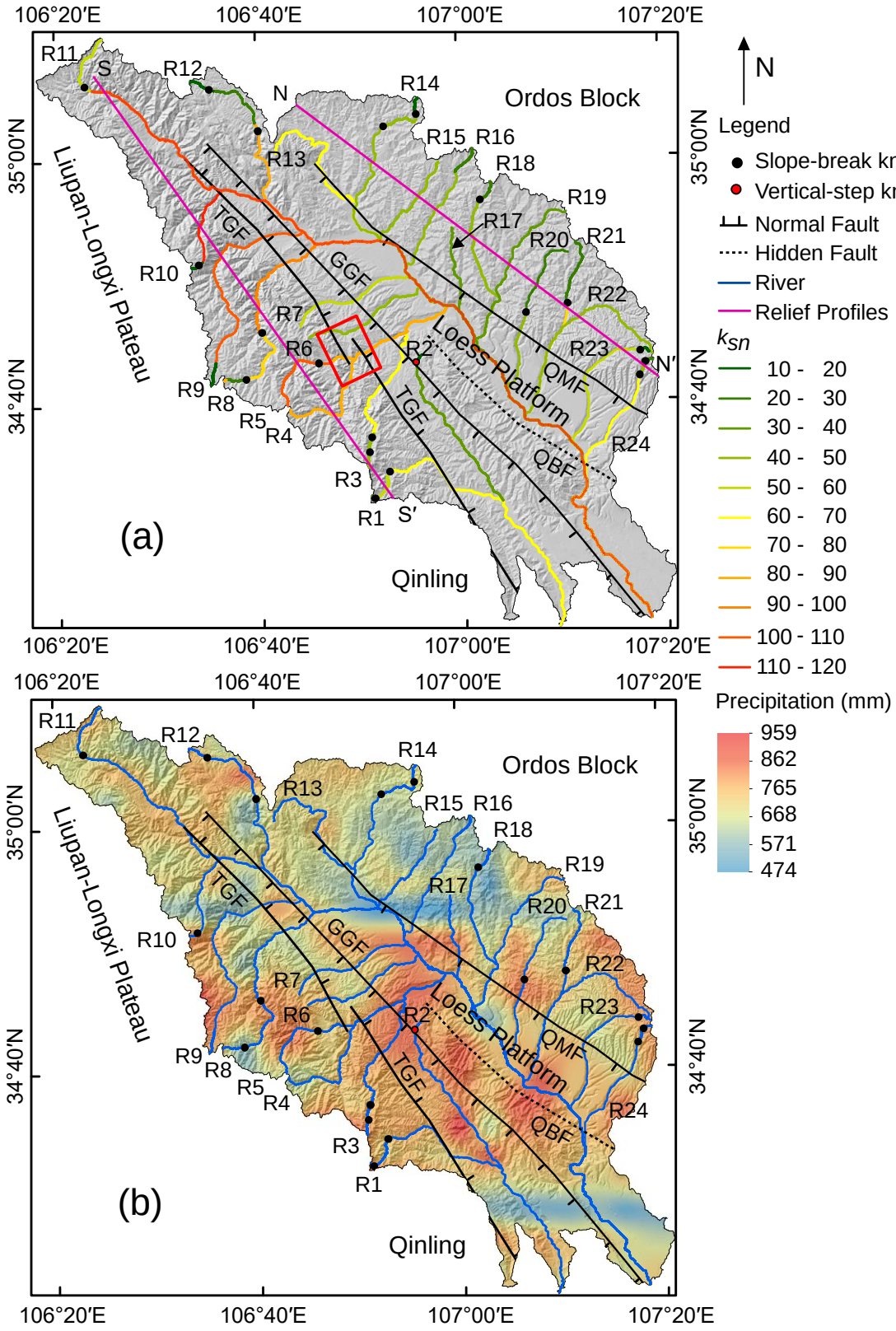

Fig. 5. (a) The distribution of main rivers and knickpoints in study area. The black points are the slope-break knickpoints and the red point is the vertical-step knickpoint. River 1 to River 11 are south rivers, River 12 to River 24 are north rivers. The red box indicates the location of potential fault linkage in the future. NN' and SS' are two profiles along the strike and paralleling the QMF and TGF. (b) Annual mean

precipitation distribution map in 2017, resampled from PERSIANN-Cloud Classification System (PERSIANN-CCS). See Fig. 1 for fault names.

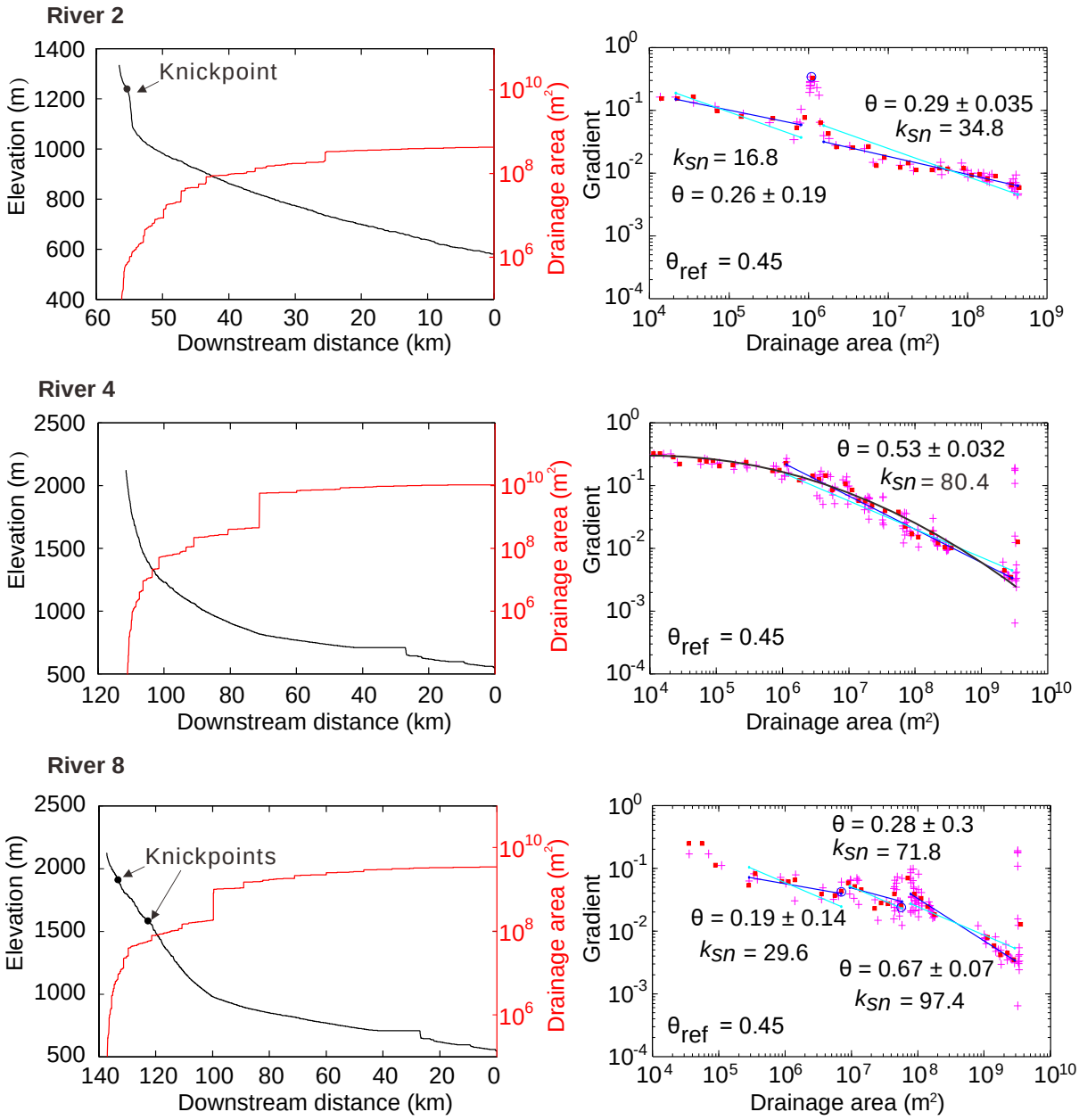

Fig. 6. The left columns show representative examples of river longitudinal profiles (black solid lines), the relationship between downstream distance and drainage area (red solid lines), and black points mark the knickpoints location. While the right columns show the SA plots extracted from SRTM1, and the concavities, θ, and normalised steepness index, k_{sn}, where θ =0.45 are also shown on the SA plots. The black line on SA plot of River 4 is log(S) curve. All these rivers show different river longitudinal profiles with vertical-step knickpoints, without knickpoints, and slope-break knickpoints, respectively.

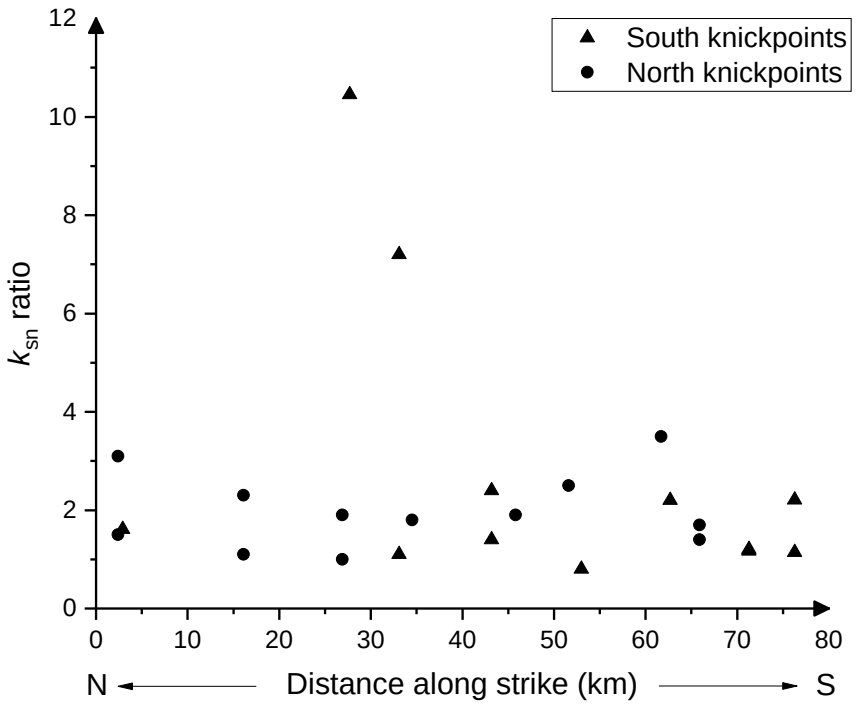

Fig. 7. The k_{sn} ratios of knickpoints along strike.

0

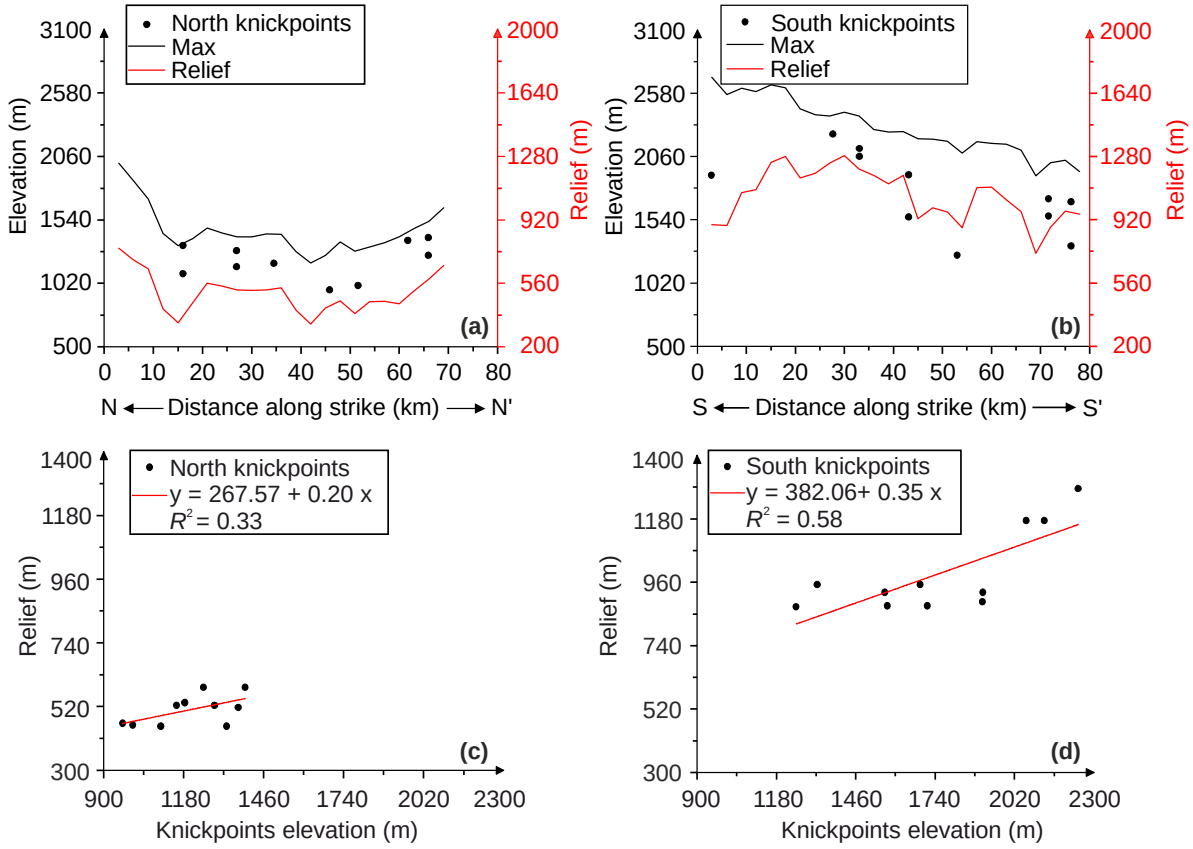

Fig. 8. The relationship between the elevation of the knickpoints and profile relief plotted along strike, which shows that there is a similar trend between the elevation of the knickpoints and relief. (a) and

(b) are the north and south profile relief along strike, respectively. (c) and (d) are the north and south profile (NN’ and SS’) relief against knickpoint elevation, respectively.

1

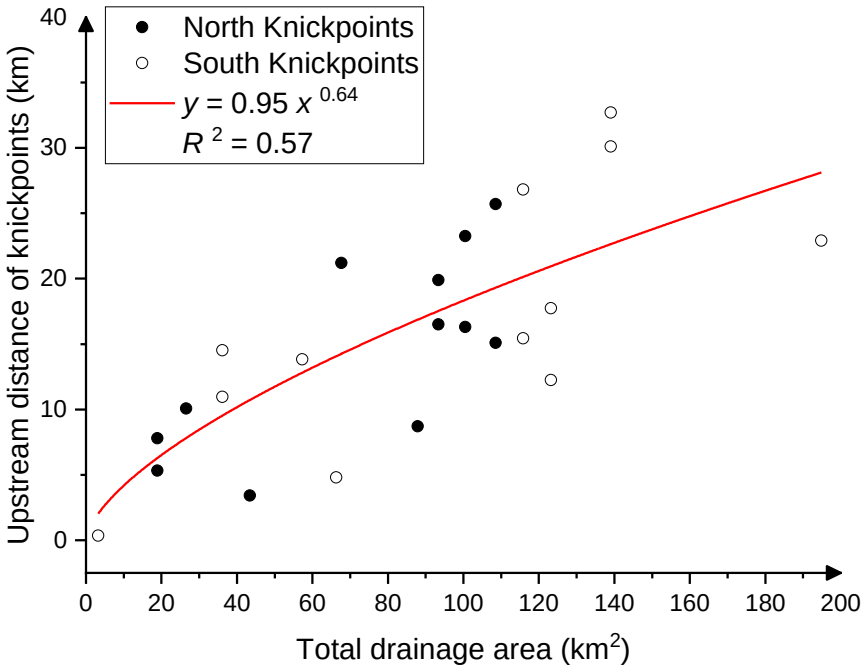

Fig. 9. The map of upstream distance from faults to knickpoints against total drainage area.

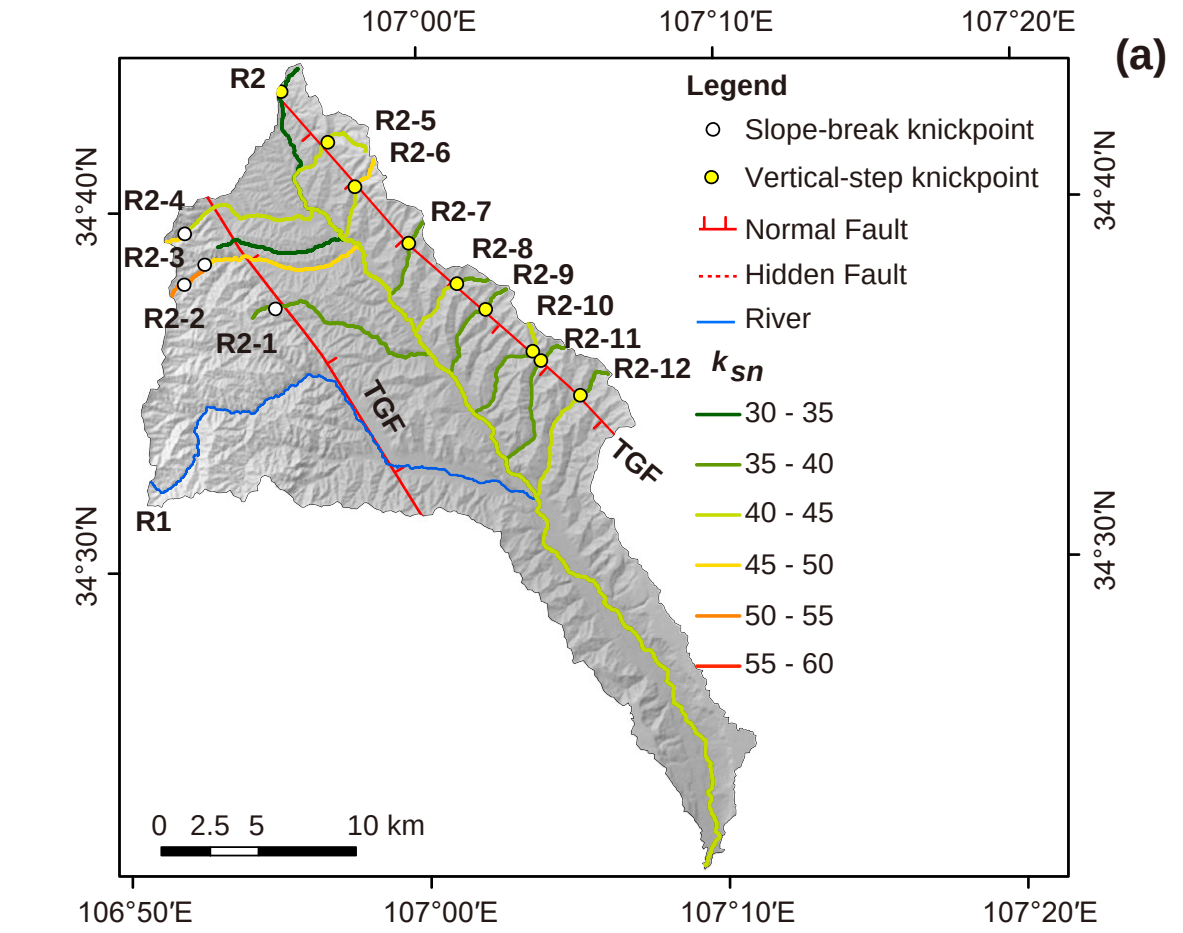
(a)
107°00′E
107°10′E
107°20′E
34°40′N
34°30′N
106°50′E
R2
R2-5
R2-6
R2-7
R2-8
R2-9
R2-10
R2-11
R2-12
R2-4
R2-3
R2-2
R2-1
R1
TGF
TGF
Legend
Slope-break knickpoint
Vertical-step knickpoint
Normal Fault
Hidden Fault
River
k_{sn}
30 - 35
35 - 40
40 - 45
45 - 50
50 - 55
55 - 60
0 2.5 5 10 km

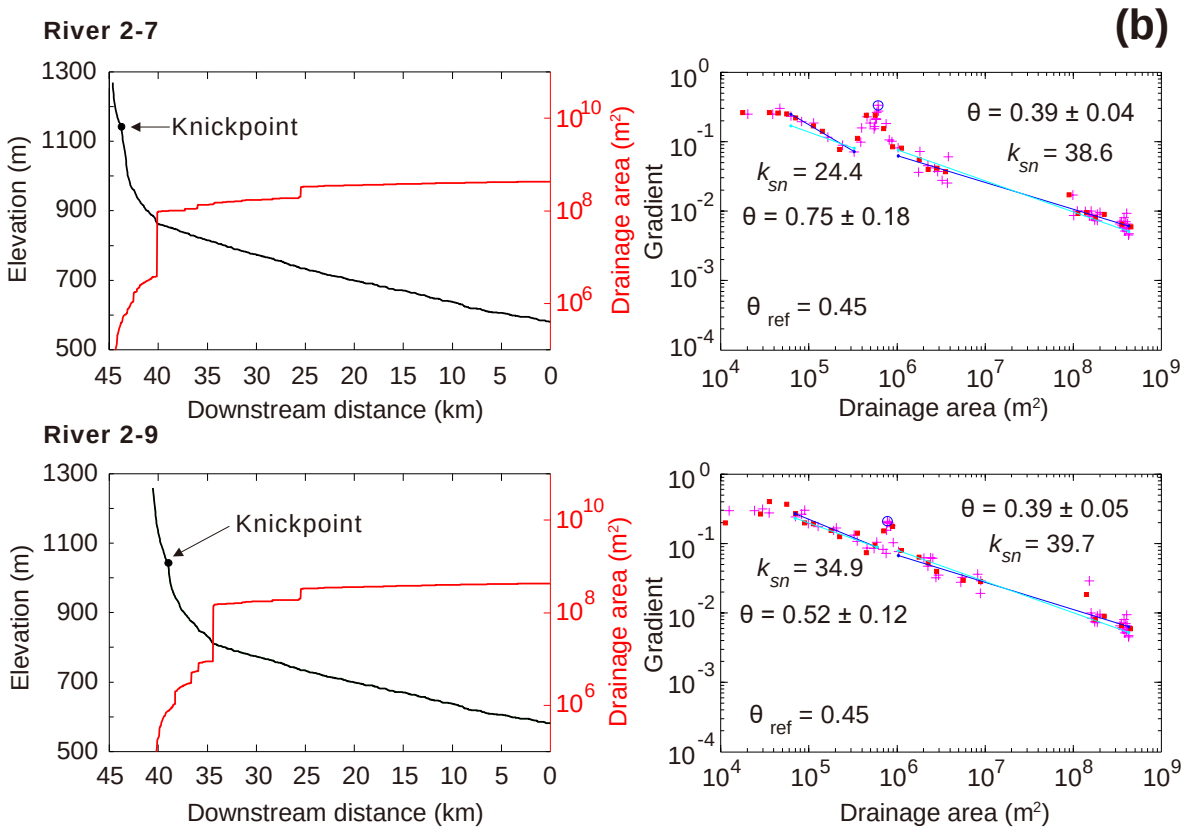
(b)
River 2-7
Knickpoint
Elevation (m)
Drainage area (m²)
Downstream distance (km)
Gradient
θ = 0.39 ± 0.04
k_{sn} = 38.6
k_{sn} = 24.4
θ = 0.75 ± 0.18
θ ref = 0.45
Drainage area (m²)
River 2-9
Knickpoint
Elevation (m)
Drainage area (m²)
Downstream distance (km)
Gradient
θ = 0.39 ± 0.05
k_{sn} = 39.7
k_{sn} = 34.9
θ = 0.52 ± 0.12
θ ref = 0.45
Drainage area (m²)

Fig. 10. (a) The topography map of Jinlinghe Graben. (b) Representative Slope-Area plots for two tributaries on northside of River 2.

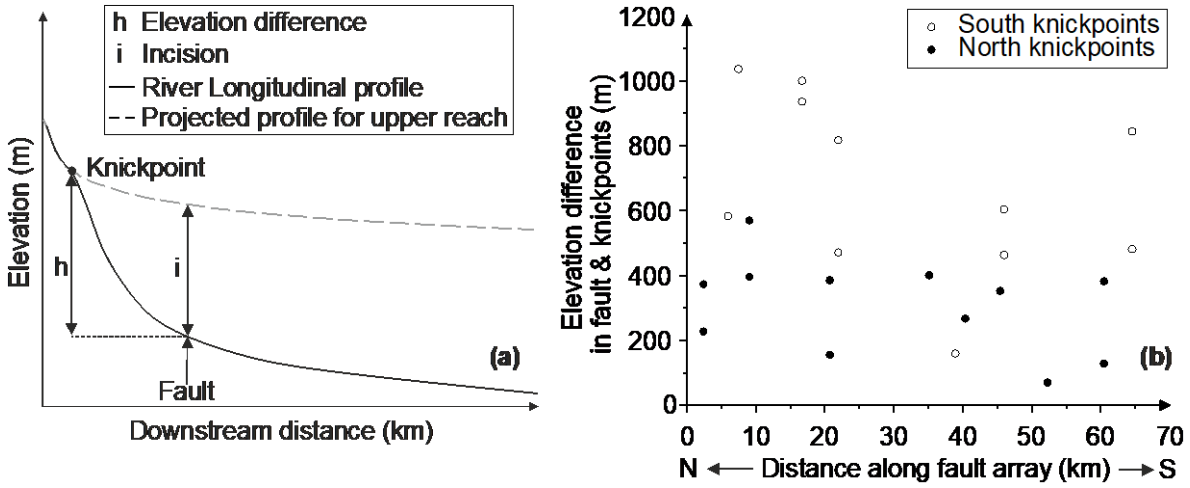

Fig. 11. (a) River longitudinal profile shows the difference between fault and knickpoints. The dashed line shows the projected profile for upper reach. (b) The elevation difference in fault and knickpoints of Qianhe Graben.

3

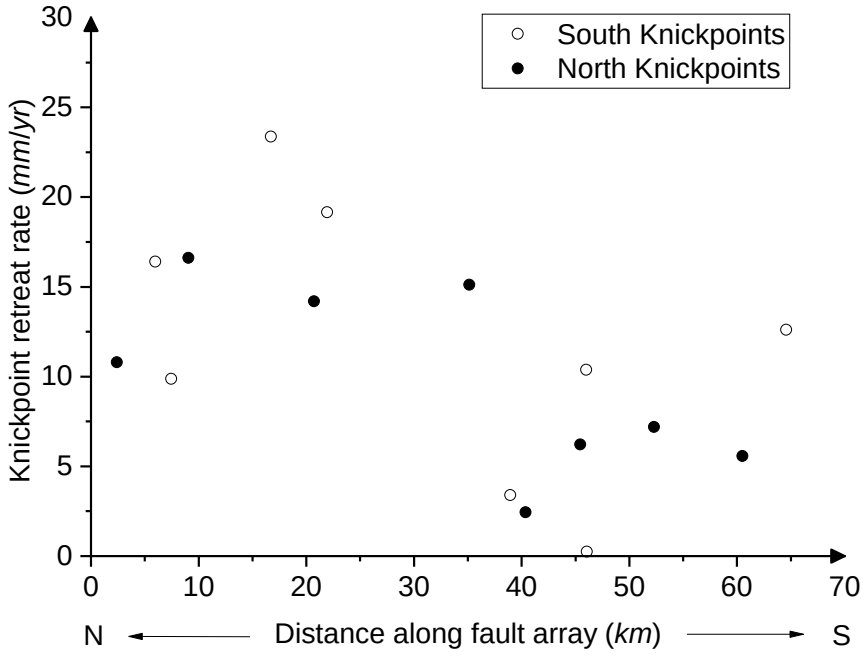

Fig. 12. Retreat rates of knickpoints (except for the lower knickpoints) along strike in this study area, showing a range of fault initiation at 1.4 Myr.

4

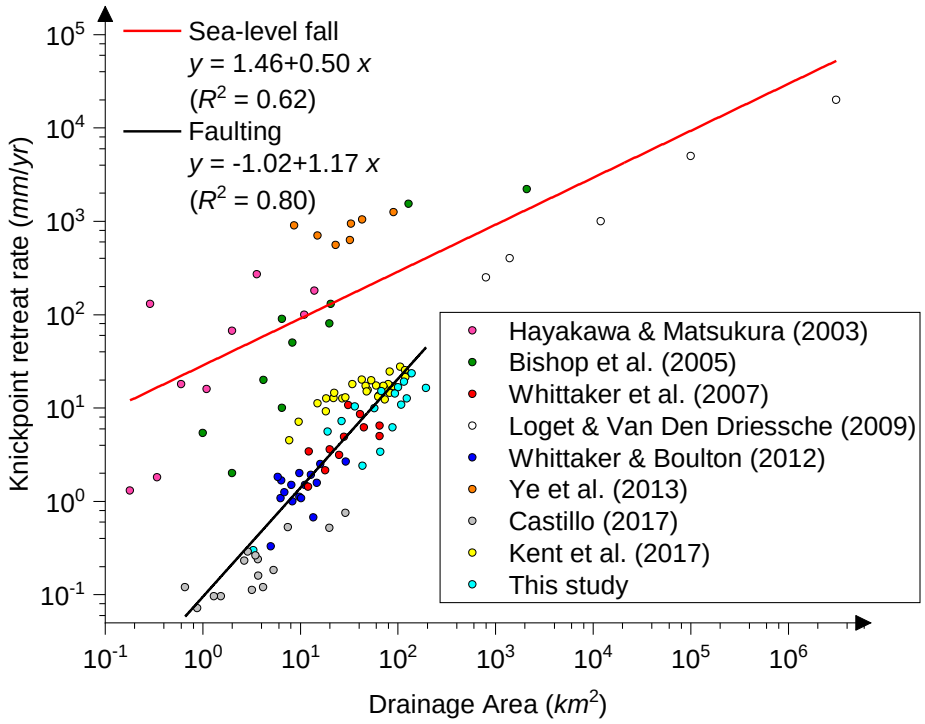

Fig. 13. The map of knickpoint retreat rates of knickpoints against drainage area in different areas. 1.4 Myr was selected as the age of the fault initiation in this study area (see text for details).

5

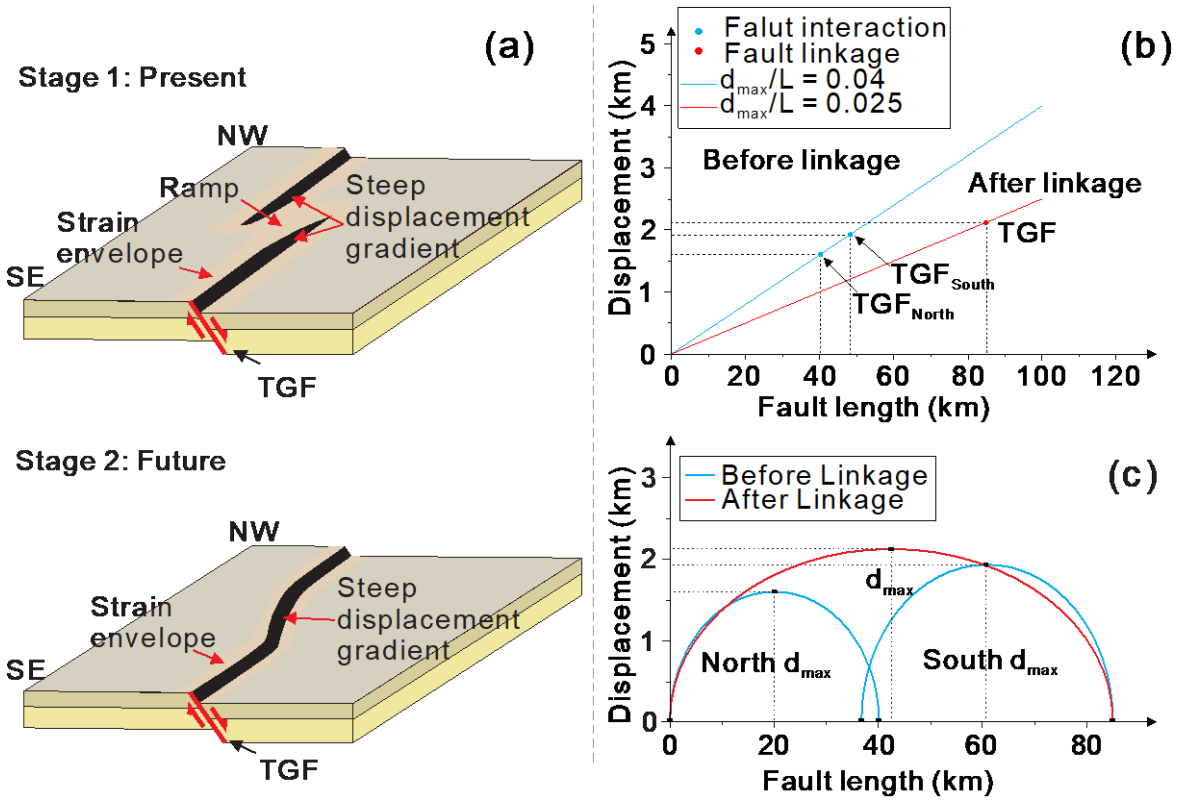

Fig. 14. (a) Plot of different states before and after fault linkage. (b) The relationship between faults length and displacement of TGF. (c) Fault linkage model (Wells and Coppersmith, 1994; Kim and Sanderson, 2005; Fossen and Rotevatn, 2016; Wang et al., 2018a).

Table 1. The statistics of extracted long rivers with knickpoints. * donates rivers with second (higher) knickpoints.

River Number	Distance along strike	river length	Relief	Active fault elevation	Total Drainage area	Knickpoint elevation	Upstream distance of knickpoints	k_{sn} above knickpoint	k_{sn} below knickpoint	k_{sn} ratio	Knickpoint retreat rate (at 1.2 Myr)	Knickpoint retreat rate (at 1.4 Myr)
	km	km	m	m	km^2	m	km	$m^{0.9}$	$m^{0.9}$		mm/yr	mm/yr
1*	76.3	54.9	952	843	123.2	1687	17.7	26.8	59.2	2.2	14.8	12.6
						1324	12.2	59.2	67.2	1.1	10.2	8.7
2	62.7	56.3	1033	1076	3.3	1119	0.4	16.8	34.8	2.1	0.3	0.3
3*	71.3	108.8	878	1109	36.2	1713	14.5	42.1	49.1	1.2	12.1	10.4
						1572	11.0	49.1	62.5	1.2	9.2	7.9
5	53.0	109.3	875	1091	66.3	1250	4.8	101.0	84.3	0.8	4.0	3.4
8*	43.2	137.2	925	1092	115.8	1909	26.8	29.6	71.8	2.4	22.3	19.1
						1562	15.4	71.8	97.4	1.4	12.8	11.0
9*	33.1	143.9	1174	1125	139.1	2125	32.7	12.9	14.7	1.1	27.3	23.4
						2061	30.1	14.7	106.0	7.2	25.1	21.5
10	27.7	134.5	1285	1209	57.3	2245	13.8	11.0	115.0	10.5	11.5	9.9
11	2.9	160.1	892	1324	194.9	1907	22.9	56.6	91.0	1.6	19.1	16.4
12*	2.4	111.0	760	1151	108.6	1720	15.1	18.6	28.0	1.5	12.6	10.8
						1546	25.7	28.0	88.1	3.1	21.4	18.4
14*	16.1	123.3	452	945	100.5	1330	23.3	20.0	43.1	2.3	19.4	16.6
						1100	16.3	43.1	45.8	1.1	13.6	11.6
16*	26.9	106.7	524	888	93.4	1288	19.9	23.7	24.6	1.0	16.6	14.2
						1155	16.5	24.6	46.8	1.9	13.8	11.8
18	34.5	93.2	534	832	67.7	1184	21.2	24.3	43.1	1.8	17.7	15.1
20	45.8	80.2	462	897	43.4	966	3.4	22.7	43.8	1.9	2.8	2.4
21	51.6	79.0		874	87.9	1002	8.7	28.6	70.8	2.5	7.3	6.2
23	61.7	61.0	517	989	26.6	1371	10.1	17.2	59.3	3.5	8.4	7.2
24*	65.9	54.6	586	1023	19.0	1395	7.8	27.5	46.7	1.7	6.5	5.6
						1250	5.3	46.7	65.7	1.4	4.4	3.8

Table 2. The information about long river profiles without knickpoints.

No	Length (*km*)	Log(S) Curve	k_{sn}	θ	±	R^2			
						Linear	Exponential	Logarithmic	Power
4	111.4	Convex	80.4	0.53	0.03	0.76	0.84	0.97	0.89
6	99.5	Linear	46.6	0.43	0.03	0.74	0.80	0.95	0.93
7	102.0	Linear	50.3	0.32	0.07	0.78	0.83	0.95	0.92
13	78.6	Convex	60.7	0.55	0.05	0.74	0.81	0.95	0.92
15	106.7	Convex	43.2	0.37	0.03	0.86	0.90	0.93	0.88
17	83.6	Linear	30.1	0.37	0.04	0.87	0.90	0.90	0.88
19	63.1	Linear	36.3	0.38	0.03	0.83	0.88	0.90	0.87
22	83.7	linear	45.9	0.26	0.04	0.85	0.92	0.93	0.83

8

Table 3. The statistics of the vertical-step knickpoints in the River 2 tributaries.

River number	River length (*km*)	k_{sn} above knickpoints	k_{sn} below knickpoints	k_{sn} ratio
R2-5	55.2	40.2	39.4	1.0
R2-6	49.4	49.9	40.8	0.8
R2-7	44.7	24.4	38.6	1.6
R2-8	42.9	29.2	40.4	1.4
R2-9	40.5	34.9	39.7	1.1
R2-10	38.6	33.0	39.1	1.2
R2-11	36.4	27.6	39.7	1.4
R2-12	34.4	26.7	42.0	1.6

9

Table 4. Statistics of knickpoints retreat rates (mm/yr) between the two sides of Qianhe Graben.

Fault	Maximum		Minimum		Mean	
	at 1.4 Myr	at 1.2 Myr	at 1.4 Myr	at 1.2 Myr	at 1.4 Myr	at 1.2 Myr
TGF	23.4	27.3	0.3	0.3	12.1	14.1
QMF	16.6	19.4	2.4	2.8	10.3	12.0

10